May 2018

Numerical Study of Oxidation in Stainless Steel Alloy Ep-823 by Liquid Lead-Bismuth Eutectic

Rajyalakshmi Palaparty
rajya.palaparty@gmail.com

NUMERICAL STUDY OF OXIDATION IN STAINLESS STEEL ALLOY EP-823 BY LIQUID LEAD-BISMUTH EUTECTIC

By

Rajyalakshmi Palaparty

Bachelor of Science in Mechanical Engineering

University of Nevada Las Vegas

2015

A thesis submitted in partial fulfillment

of the requirements for the

Master of Science in Engineering – Mechanical Engineering

Department of Mechanical Engineering

Howard R. Hughes College of Engineering

The Graduate College

University of Nevada, Las Vegas

May 2018

Thesis Approval

The Graduate College
The University of Nevada, Las Vegas

May 11, 2018

This thesis prepared by

Rajyalakshmi Palaparty

entitled

Numerical Study Of Oxidation In Stainless Steel Alloy Ep-823 By Liquid Lead-Bismuth Eutectic

is approved in partial fulfillment of the requirements for the degree of

Master of Science in Engineering - Mechanical Engineering
Department of Mechanical Engineering

Yi-Tung Chen, Ph.D.   Kathryn Hausbeck Korgan, Ph.D.
Examination Committee Chair   *Graduate College Interim Dean*

Hui Zhao, Ph.D.
Examination Committee Member

Mohamed Trabia, Ph.D.
Examination Committee Member

Zhonghai Ding, Ph.D.
Graduate College Faculty Representative

Abstract

The oxidation of stainless steel is influenced by the presence of oxygen in the surrounding medium; the oxygen reacts with the alloy to form an oxide. In certain environments, such as nuclear reactor coolant systems, minimal oxidation of the stainless steel containment functions as a protective shield from corrosive coolants such as liquid lead-bismuth eutectic.

In the current study, this minimal oxidation is evaluated for a system in which corrosion-resistant stainless steel alloy EP-823 is subject to an environment of flowing oxygenated liquid lead-bismuth eutectic at a temperature of $743\,\mathrm{K}$, whereby the thickness of the forming oxide layer is attributed to diffusion of oxygen within a plane comprised of the alloy. Fick's second law of diffusion and the advection-diffusion equation in one spatial dimension are utilized as the mathematical model. The diffusion problem attributed to the oxidation of metal alloys introduces complications in the domain due to: the change in density as the oxide is formed, the discontinuity in diffusion coefficients between the oxide and metal phases, and the occurrence of two moving boundaries – one separating the oxide and metal phase and the other, the interior unexposed boundary. These complications are resolved by transformations of: the space coordinate of the interface boundary, the calculating space coordinate, and the space coordinate of interior moving boundary. Hereby, the domain of the mathematical model is fixed. The discontinuity of the diffusion coefficients at the phase boundary is resolved by a final transformation.

The implicit numerical scheme applied to the mathematical model is described. This method, termed the 'enthalpy method', is typically used for moving boundary phase change problems. The implemented Newton-Raphson iterative technique for this finite difference method and the solution by a tri-diagonal matrix algorithm are also described.

Input parameters for the numerical simulation are derived both from physical assumptions and from controlled experiments of the oxidation of EP-823 alloy, which had been previously determined an optimal corrosion-resistant steel [1]. Such parameters include the concentration of oxygen at interface, which is determined by considering the solubility of oxygen in EP-823 alloy. The effective oxidation of the alloy is studied by assessing the oxidation of the alloys component metals. The plausible oxidation reactions and resulting oxides are compiled based on partial pressure of oxygen in lead-bismuth eutectic, temperature, and free energy of formation of the relevant oxides. Hereby, input parameters such as mass fraction of the metal in its component oxide and density of the metal were obtained. The experimentally determined scale removal rate was also used as an input. The diffusivity of oxygen in the oxide and metal phases was estimated based on the physical assumptions of higher porosity in the oxide phase.

The numerical results, which are in the form of the oxygen concentration profiles as a function distance

from the calculating space coordinate at varying time intervals, contain the the calculated corresponding oxide layer thicknesses. The results are fit to a parabolic growth rate law, whereby the the growth rate, k_p, of each relevant oxide is determined. The growth of copper (I) oxide, aluminum (III) oxide, niobium (II) oxide, and tungsten (IV) oxide demonstrate good adherence to the parabolic rate law. The numerical k_p values are benchmarked with the experimental effective k_p value for EP-823. It is determined that the experimental k_p value is closest to the numerically determined k_p values of aluminum (III) oxide and niobium (II) oxide.

From the k_p values, the steady state thickness of each oxide, δ_s, is derived by the Tedmon model for oxidation-ablation. These values are benchmarked with the semi-empirically determined steady state thickness from the mentioned controlled experiments, which is $35.8\,\mu m$, and which is found to be closest to the numerically determined δ_s value for niobium (II) oxide, at $20.1\,\mu m$.

In order to ascertain the numerically determined k_p and δ_s values, further work in assessing and optimizing stability and convergence criteria must be done.

The Pilling-Bedworth ratio for the alloying metal oxides is also calculated. The ratios suggest that aluminum (III) oxide and niobium (II) oxide, for which the respective ratios are 1.27 and 1.37, are the most stable relative to the oxides of the other alloying metals.

Furthermore, by considering selective oxidation of alloying metals, co-precipitation, oxidation states of the metals, crystal structure, and ionic radii, the likelihood of the participation of certain alloying elements in the effective oxide layer can be gauged.

Thus, it is determined that the one-dimensional planar oxidation model can be effective as a preliminary tool in assessing the oxidation of the alloy in terms of participation of its component metals. Hereby, the objectives of the study are met.

Acknowledgments

Dedication

Dedicated to my parents and to my teachers.

Table of Contents

List of Tables

List of Figures

Nomenclature

Symbol	Definition	Dimensions
$\mathbf{a}_i$	**Atomic Ratio Alloying Element** M **to Alloy**	
at.-%O	**Atomic Percent Oxygen**	
C_{MO}	**Concentration of Oxygen at Right Oxide/Metal Interface**	$[\mathbf{mol/L^3}]$
$C_{M\infty}$	**Concentration of Oxygen at Interior Front**	$[\mathbf{mol/L^3}]$
C_{OM}	**Concentration of Oxygen at Left Oxide/Metal Interface**	$[\mathbf{mol/L^3}]$
C_{O0}	**Concentration of Oxygen at Exterior Surface**	$[\mathbf{mol/L^3}]$
C_1	**Concentration of Oxygen in Oxide Phase**	$[\mathbf{mol/L^3}]$
C_2	**Concentration of Oxygen in Metal Phase**	$[\mathbf{mol/L^3}]$
D_{Me}	**Diffusion Coefficient for Oxygen in Metal Phase**	$[\mathbf{L^2/t}]$
D_{Ox}	**Diffusion Coefficient for Oxygen in Oxide Phase**	$[\mathbf{L^2/t}]$
D_0	**Maximal Diffusion Coefficient**	$[\mathbf{L^2/t}]$
E_a	**Activation Energy for Diffusion**	$[\mathbf{ML^2/t^2}]$
EP-823	**Martensitic Stainless Steel Alloy**	
f	**Left Coefficient of Tri-diagonal Matrix**	
g	**Middle Coefficient of Tri-diagonal Matrix**	
h	**Right Coefficient of Tri-diagonal Matrix**	
i	**Space Index**	
J	**Molar Flux**	$[\mathbf{mol/L^2}]$
j	**Dummy Space Index**	
K_r	**Scale Removal Rate**	$[\mathbf{L/t}]$
k	**Iterative Index**	
k_p	**Parabolic Growth Constant**	$[\mathbf{L^2/t}]$
k_0	**Maximum Parabolic Growth Constant**	$[\mathbf{L^2/t}]$
$L(t)$	**Position Coordinate of Interior Front**	$[\mathbf{L}]$
L_0	**Width of Original Specimen**	$[\mathbf{L}]$
LBE	**Liquid Lead-Bismuth Eutectic**	

Symbol	Definition	Dimensions
M	Generic symbol for Metal Element	
$\mathbf{M}_i$	Atomic Mass Alloying Element M	[**M/mol**]
M_{metal}	Atomic Mass of Metal M in M_xO_y	[**M/mol**]
$M_{M_xO_y-R}$	M atoms Oxidizing within Oxide Layer	
M_{oxide}	Molar Mass of Oxide M_xO_y	[**M/mol**]
$M_{total-R}$	Total Number of Reactive Metal M Ions	
M_xO_y	Generic symbol for Metal Oxide	
$M_{\Delta\lambda-R}$	M atoms Oxidizing within $\Delta\lambda$	
m	Dimensionless Factor	
N	Number of Nodes in Spatial Interval	
n	Time Index	
$\mathbf{n}$	Number of Atoms M per Molecule Metal Oxide	
$\mathbf{P}_{O_2}$	Partial Pressure of Oxygen in LBE	[$\mathbf{ML^{-1}t^{-2}}$]
p	$M_{\Delta\lambda-R}/M_{total-R}$	
$1-p$	$M_{M_xO_y-R}/M_{total-R}$	
Q	Activation Energy for Oxidation	[$\mathbf{ML^2mol^{-1}T^{-1}t^{-2}}$]
$Q(C_j^k)$	Function in Right Side of Tri-diagonal Matrix Equation	
R	Universal Gas Constant	[$\mathbf{ML^2mol^{-1}T^{-1}t^{-2}}$]
R_{PB}	Pilling-Bedworth Ratio	
r	Mass Fraction of M in M_xO_y	
T	Absolute Temperature	[**T**]
t	Time Coordinate	[**t**]
t_{exp}	Experimental Time	[**t**]
V_{Me}	Velocity of Interior Front	[**L/t**]
V_{OM}	Velocity of Oxide/Metal Interface	[**L/t**]
w	Weight Ratio of Element M in Metal Alloy	
$\mathrm{w_i}$	Mass Alloying Element M per $100\,\mathrm{g}$ Alloy	
wt.-%C	Weight Percent Carbon	
wt.-%O	Weight Percent Oxygen	
X	Total Moles Alloying Element M per $100\,\mathrm{g}$ Alloy	[**mol/M**]
$\mathrm{X_i}$	Moles Alloying Element M per $100\,\mathrm{g}$ Alloy	[**mol/M**]
x	Position Coordinate	[**L**]
Z	Kirchhoff Transformation Variable	

Symbol	Definition	Dimensions
Δy	**Width Between Nodes**	**[L]**
$\Delta \delta_{in}$	**Change in thickness of Inner Oxide Layer**	**[L]**
$\Delta \delta_{out}$	**Change in thickness of Outer Oxide Layer**	**[L]**
$\Delta \delta_{tot}$	**Change in thickness of Total Oxide Layer**	**[L]**
$\Delta \lambda$	**Layer Width in which all $M_{total-R}$ are Located**	**[L]**
$\delta(t)$	**Position Coordinate of Oxide/Metal Interface**	**[L]**
δ_{exp}	**Experimental Oxide Layer Thickness**	**[L]**
δ_{in}	**Inner Oxide Layer Thickness**	**[L]**
δ_{out}	**Outer Oxide Layer Thickness**	**[L]**
δ_s	**Asymptotic Oxide Layer Thickness**	**[L]**
ϵ	**Convergence Accuracy**	
ρ_{Me}	**Density of Metal Alloy**	**[M/L^3]**
ρ_{oxide}	**Density of Metal Oxide M_xO_y**	**[M/L^3]**
ρ_{metal}	**Density of Metal M in M_xO_y**	**[M/L^3]**
ρ_{in}	**Density of $\Delta \delta_{in}$**	**[M/L^3]**
ρ_{out}	**Density of $\Delta \delta_{out}$**	**[M/L^3]**
$[0, a]$	**Spatial Interval**	**[L]**

Chapter 1 Introduction

1.1 Material Degradation

Material degradation is defined as the loss of performance of an engineering system. The factors involved in degradation are losses of mechanical strength, efficiency, lifetime, and appearance of a system. Wear and the need for tedious and expensive control of these losses are also included in the definition. The direct and indirect costs related to loss, replacement, and prevention of material degradation are significant. In the year 2013, the estimated annual cost of material degradation for the United States alone is $500 billion [2]. More importantly, material degradation eventually causes potential failure or contamination of systems leading to the impairment or loss of human life. Because these economic and societal impacts should not be ignored, the rigorous study of material degradation is essential.

With respect to the study of material degradation, metals are generally distinguished from non-metals. One main form of metal degradation is the corrosion of metals and metal composites. The topic of corrosion is divided into: contributing factors, high temperature corrosion, measurement, characteristics, forms, and control processes in prevention [3]. The purpose of a corrosion control process, which is the broad topic of the current study, is to ensure longevity of the metal or metal composite.

The study of control processes in prevention of corrosion involves: material selection, design, electrochemical protection, coating, passivation, and operating environment [4]. In the current study, the relationship among material selection, operating environment, and passivation is researched. The composition of the structural material is determined by metallurgical techniques. The resulting mechanical factors, such as stress or the presence of non-reactive impurities, either promote or inhibit corrosion. The chemistry attributed to the composition also affects corrosion. The medium of the operating environment is either semi-solid, such as soil, or fluid, such as air or water. To address corrosion control in an aqueous medium such as water or liquid metal, temperature, pH, partial pressure and concentration of dissolved oxygen, presence and formation of ions, velocity, and conductivity of the medium are regulating factors [5]. By monitoring and adjusting these factors and choosing the correct structural material, limited surface corrosion of a metal or metal composite can be maintained at an optimal thickness to prevent further corrosion. This process is referred to as passivation.

1.2 Passivation

In order to discuss passivation of metals and metal composites, the concept of corrosion is further described. Metals and metal composites used in engineering systems are refined and/or purified forms (e.g. stainless steel) of naturally occurring metal oxides (e.g. iron ore, hematite and magnetite). From a practical

perspective, corrosion can be defined as the tendency of the refined metal to revert back to its original metal oxide phase. This process occurs via an electrochemical reaction between the metal and its environment; this involves the transfer of electrons from the metal by two half cell reactions: one anodic or oxidizing, and the other, cathodic or reducing. By losing these electrons, the metal loses mass – whereby degradation begins [4]. Thus, the scientific definition of corrosion is the electrochemical degradation of metals and metal composites.

The film of a corrosion resistant surface, or passivated surface, experiences a certain region of anodic and cathodic polarization, both of which are directly attributed to a specific range of ion current density and pH. The stabilizing ion current density and stabilizing pH are maintained by conditions which are specific to: metal, solution, temperature, the degree of reducing atmosphere, and whether ablasion of the surface occurs [4]. Furthermore, in order for a stable passivating layer to be achieved, the rate of metal oxide formation must exceed that of metal dissolution in the surrounding fluid [6]. The interface of the corrosion resistant film and un-oxidized metal is considered anodic because it is the location where oxidation of the metal occurs as a result of inward oxygen ion diffusion from the surrounding medium. Alternately, the cathodic side occurs at the exposed surface of the film because it is the site of the reduction of outward migrating metal ions. In this manner, the oxide layer functions as both a conductor and an electrolyte [4].

If the assumption is made that oxide layer growth is guided primarily by the reaction at the anodic side, then the formation of the passivating layer can be correlated to inward oxygen diffusion. In other words, if oxidation is rate controlling with respect to the total oxidation-reduction system, then the formation of the oxide layer is dependent on the migration of oxygen ions from the fluid to the interface of the oxide and the metal. This flux of oxygen ions is mathematically modeled via Fick's laws of diffusion, from which a parabolic growth rate of the oxide layer is derived. Hereby, the diffusion of oxygen ions into the metal is modeled as a means of determining the passivation capacity of the resulting oxide layer.

In order for passivation to occur, it is presupposed that the surrounding medium contains a concentration of oxygen which influences oxidation such that the oxide layer thickness is protective. An example of such media are liquid lead alloy coolants, such as lead-bismuth eutectic (LBE), which are commonly used in nuclear reactor coolant systems. Due to the corrosive nature of the liquid lead alloys on the containment (primarily a design consisting of stainless steels), maintaining an optimal oxygen level to promote passivation of the stainless steel is ideal in avoiding critical safety issues in nuclear reactor environments [6]. By monitoring diffusion of oxygen from the coolant medium into the stainless steel, whereby an oxide layer is formed, the optimal oxygen concentration level in the medium is determined.

1.3 Literature Review

The selected literature for the survey is discussed. As per the present model, the assumptions and mathematics of planar diffusion with respect to Fick's diffusion laws have been described extensively by Crank [7]. Based on the assumptions made, Crank has explained diffusion with respect to topics such as moving boundaries or interfaces, the definition and measurement of discontinuous diffusion coefficients, and finite difference methods. These topics directly relate to the present diffusion model.

The moving interface in the present model designates the phase change from metal to oxide. As oxidation progresses, the location of this interface moves inward from the original surface of the metal. A model of a travelling phase change boundary in two-phases has been solved by Stefan with respect to heat flux. The Stefan solution has been outlined by Merimanov and Hill [8, 9].

Furthermore, the solutions of heat flux within a composite sheet comprised of two layers for which the thermal conductivities are different have been solved by Carslaw and Jaeger [10]. Both the Stefan solution and that of Carslaw and Jaegar have been employed by Crank to develop a solution for planar diffusion in both metal and oxide phases which are separated by a moving boundary and for which the diffusion coefficients differ [7]. For mathematical simplicity, transformations of moving boundary value problems into stationary boundary value problems have been formulated by Landau [11]. By transforming the coordinate of the moving boundary into a fixed boundary, the application of this method immobilizes the domain of the boundary value problem [11].

A parabolic growth rate for metal oxidation has been proposed by Wagner. It is derived from Fick's law in which Wagner has considered chemical potential, activity, and motility of oxygen anions [12]. Wagner also has considered density change in the domain occuring as a result of both metal oxide formation and uneven distribution of cations in the resulting layer [12]. Wagner has concluded that this discontinuity is a complicating factor in oxidation-diffusion moving boundary problems. Coates and Dalvi confirm this complication in an extension of Wagner's theories to the various alloys [13]. An oxidation model combining Wagner's parabolic rate law and a linear term representing the volatilization of Fe-Cr alloys in air has been developed by Tedmon et al. [14]. With respect to heat conduction, the asymptotic growth of the moving boundary layer which has been formulated by Stefan is outlined by Hill [9].

As mentioned, finite difference method applications for the two phase diffusion model have been described by Crank [7]. Crank has explained how the Crank-Nicholson method and the other methods are to be used to numerically solve the diffusion model. Ding and Lagoudas have applied a coordinate transformation inspired by Landau's method to one-dimensional diffusion problems in planar, cylindrical and spherical geometries [15]. By implementing an implicit numerical method with respect to the transformed boundary

value problem, the oxidation of titanium has been simulated and benchmarked with experimental data; the results were found to be in good agreement with the experimental data [15]. Shamsundar and Sparrow have examined the density change effect of metal oxidation on solutions of moving boundary conduction problems [16]. Both complications of change in density and the moving boundary have been resolved by Wong and Chan by a special coordinate transformation which is likened to the mentioned Stefan solution in heat transfer [17]. An implicit finite difference code using the Newton-Raphson iterative method has been used to simulate the oxidation of a zirconium alloy in steam [17]. Tan has developed a mathematical model for one-dimensional planar diffusion wherein the parabolic oxide layer growth rate is combined with a linear oxide scale removal rate resulting from erosion or ablation of the oxide surface [6]. The density changes in both the metal and oxide phase have been considered and incorporated into the model which thus accounts for volume expansion. A coordinate transformation, similar to Wong's, has been applied to arrest the interior moving boundary of the unexposed surface. An implicit finite difference scheme utilizing the Newton-Raphson iterative model has been applied to the transformed boundary value problem [6]. The resulting code has been used to simulate the oxidation of titanium and zirconium, the results of which have been compared to the results obtained by Ding and Lagoudas as well as available experimental data [6, 15].

The main experimental research literature surveyed is that of Zhang. The experiments conducted herein involved subjecting different steel alloys to typical nuclear reactor coolant environments [1]. Zhang has incorporated scale removal into the Tedmon model in order to approximate steady-state oxide layer thicknesses from experimental oxide layer thicknesses for each alloy tested [1].

1.4 Motivation for Study

The motivation of the present study is to investigate the impact of stainless steel composition on passivation in typical nuclear reactor coolant system environments. Specifically, modelling oxidation of the corrosion-resistant stainless steel alloy EP-823 by lead bismuth eutectic is the overall focus. The following objectives are outlined in light of this motivation.

1. In Chapter 2, after making reasonable assumptions which have a physical basis, a mathematical model of the one-dimensional planar oxidation-diffusion problem with moving phase boundaries is to be articulated.

2. In Chapter 3, the objective is to describe the numerical method applied to the mathematical oxygen-diffusion model.

3. In Chapter 4, the manner in which input parameters for the numerical simulation are derived and justified based on both physical assumptions and results of a controlled experiment conducted on

EP-823 stainless steel is delineated; the goal is to numerically simulate this controlled experiment by resolving the oxidation of the alloy into the individual oxidation-reactions of its component alloying metals.

4. In Chapter 5, the numerical data from the simulation are evaluated with three main objectives. The first is to determine the growth rate of the resulting oxide layer of each alloying element and compare it to the effective experimental growth rate determined for EP-823. The second is to apply the Tedmon equation for oxidation-ablation to the growth rate to determine the steady state thickness of the resulting oxide layer and then compare this thickness to the corresponding experimental value. The final objective is to examine selective oxidation by comparing free energy of formation, Pilling-Bedworth ratio, and the oxidation states of the alloying elements in the respective oxides.

5. In Chapter 6, by the comparisons made in Chapter 5, in conjunction with consideration of the Pilling-Bedworth ratio, selective oxidation, oxidation states and crystal structures of the alloying metal oxides, a determination of the efficacy of the one-dimensional oxygen-diffusion model as a useful tool in deciding the passivation capacity of an alloy is made.

Chapter 2 Theory

2.1 One-Dimensional Planar Oxidation

The oxidation of metals and metallic alloys is a process both chemical and physical in nature. Atomic diffusion of oxygen from the surrounding fluid into the metal or alloy, atomic inter-diffusion of alloying elements within the domain of the metal or alloy, and outward atomic diffusion of alloying elements into the surrounding fluid are essential to the process of oxidation. For the current discussion, diffusion is defined as the spontaneous transport of atoms in response to a concentration gradient of said atoms. The chemical reaction of oxidation is assumed to be so fast that the rate of oxidation is controlled entirely by diffusion [7]. Furthermore, it is assumed that the rate of outward diffusion, or flux, of the alloying elements is orders of magnitude greater than the inward flux of atomic oxygen [6]. Based on these assumptions, the entire oxidation process is limited by the one-way, inward transport of atomic oxygen from the surrounding fluid. Hereby, the diffusion pattern of oxygen within the metal alloy is correlated to the thickness of the resulting oxide layer. A diffusion model is achieved by monitoring the oxygen concentration within the alloy with respect to both distance from its surface of and time.

Prior to initial diffusion of oxygen, the region of the metal alloy being considered is assumed to be comprised of a single isotropic material free of oxygen as shown in Figure 1. As diffusion or sorption begins,
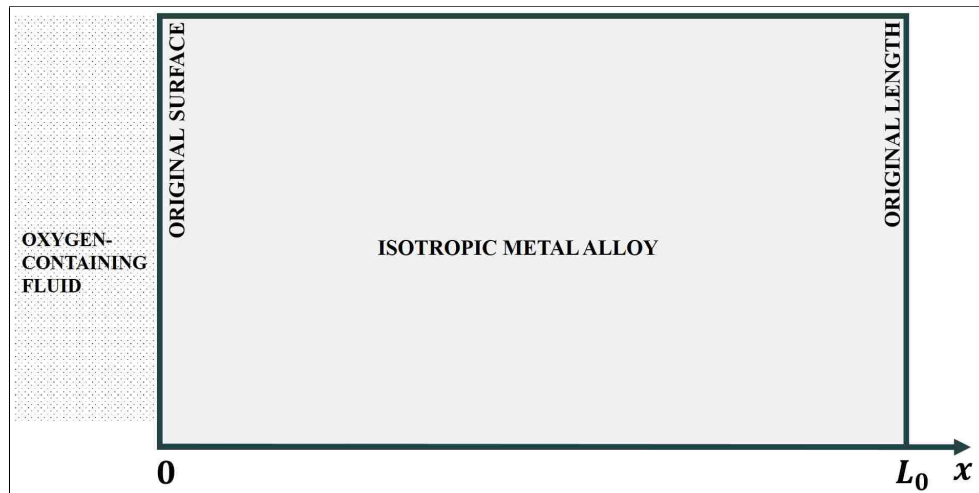
Figure 1: Oxygen-Free Material Prior to Diffusion

this region becomes a composite zone of two distinct layers: the oxide layer and the un-oxidized metal alloy layer, as shown in Figure 2. Each of these regions is assumed to be isotropic within its respective layer. A sharp interface adjoining the layers is assumed to be normal to the spatial direction, x. This assumption presumes a uniform flux of oxygen atoms through all planes normal to the spatial direction, x. In turn, this
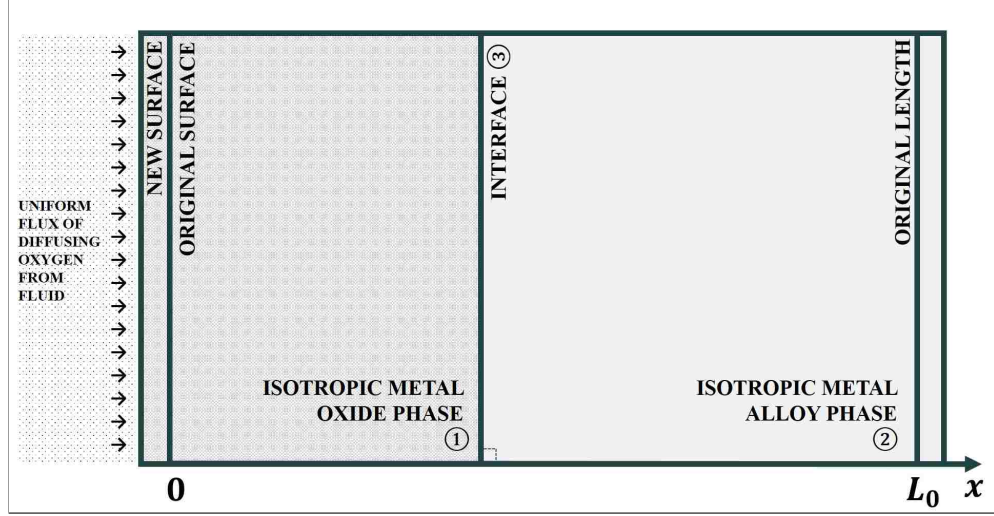
Figure 2: Layers Formed via Diffusion

causes a uniform growth of the oxide layer which is separated from the metal alloy layer by the adjacent interface. Because the tendency of oxygen to diffuse through the oxide layer varies from oxygen diffusivity in the metal alloy layer, the concentration of oxygen is separately considered for each layer.

2.2 Mathematical Model of One-Dimensional Planar Oxidation

The concentration of oxygen, C_2, in the metal phase is represented by the advection-diffusion equation (1) [7].

$$\frac{\partial C_2(x,t)}{\partial t} = D_{Me}\frac{\partial^2 C_2(x,t)}{\partial x^2} - V_{Me}\frac{\partial C_2(x,t)}{\partial x} \tag{1}$$

The concentration can also be referred to as molar density. The variables x and t are the position coordinate, measured normal to the exposed alloy surface, and time, respectively. This equation can be derived from the continuity equation, which states that the rate of change for a scalar quantity, presently concentration, in a differential control volume is given by the sum of net flux, generation, and consumption of the scalar quantity within the differential volume element. In the present case, two sources of net flux exist: namely diffusive flux and advective flux. The left hand side of equation (1) expresses the rate of accumulation or depletion of the oxygen concentration; the first term in right hand side of equation (1) represents the diffusion of oxygen, in which the proportionality constant, D_{Me}, is the diffusion coefficient of oxygen in the metal phase. The product of D_{Me} and the local curvature, which gives the local minima and maxima of oxygen concentration with respect to space, is the expression for diffusion of oxygen. The advection term is given by the second term on the right hand side of equation (1). Advection can be defined as the transport of a substance due to bulk motion. For the case of oxidation of metallic alloys, advection occurs as a result of the change in

density of the portion of the metallic alloy which experiences oxidation. In general, the oxides of the alloying elements are less dense than the alloying elements; thus, oxidation of the alloy is accompanied by an increase in volume in the region where the reaction takes place. In order to accommodate this increase in volume, the un-oxidized portion of the alloy experiences a shift, which is characterized by the velocity of its moving front, denoted V_{Me}. The surface of this moving front, the x-coordinate of which is given by $L(t)$, is always normal to the spatial direction x. The product of the first partial derivative of the concentration of oxygen with respect to position, which gives the change in concentration as a function of location, and V_{Me} is the expression for advection. The term V_{Me} is described first in terms of $L(t)$ [6]. If L_0 represents the original width of the metal alloy, then V_{Me} is given by

$$V_{Me}(t) = \frac{L(t) - L_0}{t}. \tag{2}$$

It is assumed that neither generation nor consumption of oxygen are inherent in the oxidation process. To summarize, the advection-diffusion equation predicts how the combination of diffusion and advection causes a change in concentration with respect to time.

The concentration of oxygen, C_1, in the oxide phase is modeled using Fick's second law (3),

$$\frac{\partial C_1(x,t)}{\partial t} = D_{Ox} \frac{\partial^2 C_1(x,t)}{\partial x^2} \tag{3}$$

which is a special case of the advection-diffusion equation, wherein no advection term is present. Because the oxidation takes place in the entire domain of the oxide phase, the bulk movement of the oxide phase is neglected [6]. The left hand side of equation (3), which describes the rate of change in the oxygen concentration, is proportional to the local curvature of the concentration gradient, or the second partial derivative of concentration with respect to position as given by the right hand side of equation (3). The proportionality constant, D_{Ox}, represents the diffusion coefficient of oxygen in the oxide phase. The product of the local curvature and D_{Ox} is the expression for diffusion of oxygen. To restate, Fick's second law predicts how diffusion causes a change in concentration with respect to time.

Each of the equations, (1) and (3), can only be applied to diffusion within an isotropic material, so that the flow of oxygen at any point is normal to the surfaces of constant concentration through the point due to symmetry [7]. For the purpose of one-dimensional planar modeling of oxygen diffusion, equations (1) and (3) are partial differential equations in a single Cartesian spatial dimension, x. To rephrase, the concentration gradient of oxygen only exists along the x-axis in this case. Thus, the oxygen diffuses only in the positive x-direction.

While the diffusion coefficient in solids is predicted to be a function of temperature by the Arrhenius relation

$$D = D_0 e^{-(E_a/RT)} \tag{4}$$

where D_0 is the maximal diffusion coefficient at infinite temperature, E_a is the activation energy for diffusion, T is the absolute temperature, and R is the universal gas constant, the diffusion coefficients in the present model, D_{Ox} and D_{Me}, are assigned constant values. This is due to the fact that the present model does not directly incorporate changes in temperature. A general case of diffusion coefficient, D, is also understood as the magnitude of the molar flux, J, through a surface per unit concentration gradient from Fick's first law of diffusion,

$$J = D\frac{\partial C}{\partial x} \tag{5}$$

For the time being, the diffusion coefficient changes discontinuously from one constant value, D_{Ox}, to another constant value, D_{Me}, at a certain concentration level of oxygen which corresponds to the x-coordinate of the interface adjoining oxide and metal alloy layers. Because two constant values are assigned, the present oxidation model can be called an isothermal oxidation model with binary diffusivity. The selection of the constant values for D_{Ox} and D_{Me} will be discussed later.

The values of C shown in Figure 3 are set at the following locations in the model in order to provide the boundary conditions for equations (1) and (3). The concentration of oxygen, C_{O0}, in the surrounding fluid at the original surface of the reacting metal alloy, where $x = 0$, is assumed to be at constant continuous saturation [18]. As such, diffusion of oxygen in the surrounding fluid is not considered in the model [6]. As the x-coordinate approaches the oxide/metal alloy interface from this point, the oxygen concentration decreases to the critical oxygen concentration for oxide formation, C_{OM}, which is experimentally determined [15]. For purposes of this oxidation model, C_{OM} is assigned the atomic percent of oxygen in the type of metal oxide assumed to form at the interface. At this x-coordinate point, a finite disappearance in oxygen concentration occurs. This negative jump in concentration is bound on the lower end by the solubility limit of oxygen in the metal alloy which is denoted C_{MO}. The x-coordinate of this discontinuity is the exact location of the interface between oxide and metal alloy and is denoted $\delta(t)$ because its position changes as a function of time. As such, C_{O0} and C_{OM} will serve as the lower and upper bounds for oxygen concentration, C, in equation (3). C_{MO} is the lower bound for oxygen concentration in equation (1) while the upper bound is represented by $C_{M\infty}$. The exact values of C_{O0}, C_{OM}, C_{MO} and $C_{M\infty}$ are specified later.

Due to the discontinuity in oxygen concentration at the interface which cannot be directly expressed by the two underlying partial differential equations (1) and (3), a third equation is necessary for closure. This condition, which functions like the Stefan Condition for heat conduction [9], models the velocity of

the moving interface, $\frac{d\delta(t)}{dt}$, as a function of quantities obtained from both sides of the interface which are constrained by the conservation of mass. These quantities are the mass fluxes at the location of the interface. The moving interface is expressed by equation (6) as

$$D_{Ox}\frac{\partial C_1(\delta(t),t)}{\partial x} = D_{Me}\frac{\partial C_2(\delta(t),t)}{\partial x} - |C_{OM} - C_{MO}|\frac{d\delta(t)}{dt}, \quad t > 0. \tag{6}$$

This equation can also be regarded as a mathematical statement of the discontinuous change in the diffusion coefficient accompanied by a discontinuity in the concentration gradient [7]. The mass flux from the oxide layer, $D_{Ox}\frac{\partial C(\delta(t),t)}{\partial x}$, is set equal to the sum of the mass flux from the metal alloy layer, $D_{Me}\frac{\partial C(\delta(t),t)}{\partial x}$, and the product of the negative jump in oxygen concentration, $|C_{OM} - C_{MO}|$, and the velocity of the moving interface, $\frac{d\delta(t)}{dt}$. The velocity is assigned variable V_{OM} given by

$$V_{OM}(t) = \frac{d\delta(t)}{dt}. \tag{7}$$

The governing equations for each phase and the boundary conditions are shown in Figure 3.
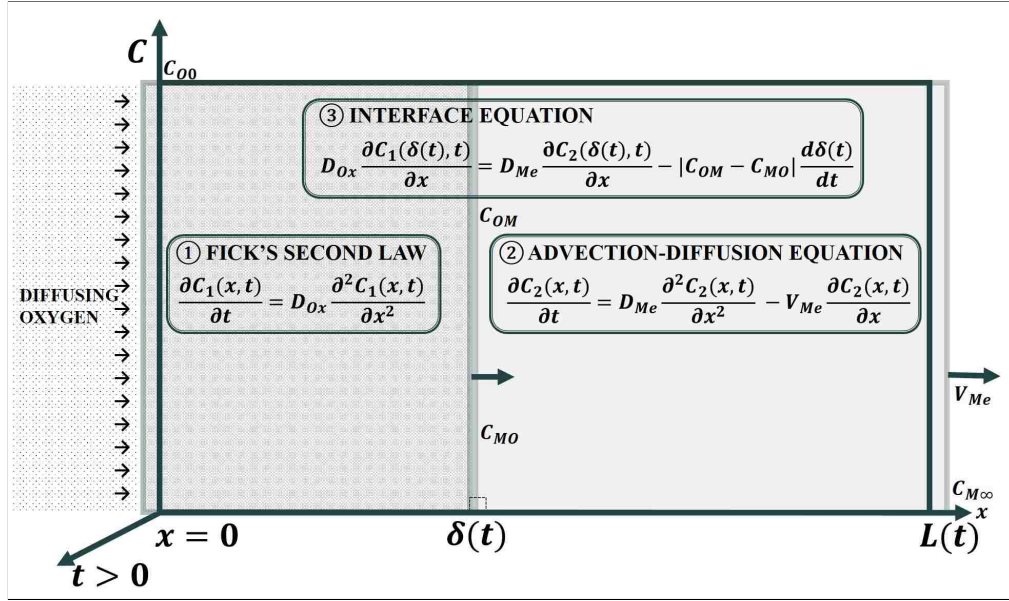
Figure 3: Governing Equations for Oxygen Concentration, C, w.r.t. x and t

The initial conditions are considered next. Because the interface initially coincides with the original un-oxidized surface of the alloy, initial oxide layer concentration, $C_1(x,0)$, is unavailable [15]. Based on the earlier assumption that the material is initially free of oxygen, a reasonable condition is

$$C_1(x,0) = 0, \quad 0 < x < \infty. \tag{8}$$

10

The x-coordinate of the interface and the initial oxygen concentration in the metal alloy layer at $t = 0$ are given by

$$\delta(0) = 0, \quad C_2(x,0) = 0 \quad for \quad 0 < x < \infty. \tag{9}$$

So far, the planar model for two-phase oxidation of metal alloys has been described. The governing equations are summarized in Table 1.

Table 1: Governing Equations for Planar Diffusion Model for Oxidation

Phase	Oxide Layer	Metal Layer	Interface
Equation Name	Fick's Second Law	Advection-Diffusion	Interface Condition
Governing Equations (t > 0)	$\frac{\partial C_1(x,t)}{\partial t} = D_{Ox} \frac{\partial^2 C_1(x,t)}{\partial x^2}$	$\frac{\partial C_2(x,t)}{\partial t} = D_{Me} \frac{\partial^2 C_2(x,t)}{\partial x^2} - V_{Me}(t)\frac{\partial C_2(x,t)}{\partial x}$	$\frac{D_{Ox}\frac{\partial C_1(\delta(t),t)}{\partial x} - D_{Me}\frac{\partial C_2(\delta(t),t)}{\partial x}}{|C_{MO}-C_{OM}|} = \frac{d\delta(t)}{dt}$
		where $V_{Me}(t) = \frac{L(t)-L_0}{t}$	where $V_{OM}(t) = \frac{d\delta(t)}{dt}$
x-domain	$0 < x < \delta(t)$	$\delta(t) < x < L(t)$	
Boundary Conditions	$C_1(0,t) = C_{O0}$ $C_1(\delta(t),t) = C_{OM}$	$C_2(\delta(t),t) = C_{MO}$ $C_2(L(t),t) = C_{M\infty}$	$C_1(\delta(t),t) = |C_{OM} - C_{MO}| + C_2(\delta(t),t)$
Initial Condition	$C_1(x,0) = 0, 0 < x < \infty$	$C_2(x,0) = 0, 0 < x < \infty$	$\delta(0) = 0$

2.3 Derivation Interface Velocity

The following describes first how V_{OM} is expressed in terms of relevant parameters. Next, V_{Me} is conveyed in terms of V_{OM}. Linking these velocities simplifies the spatial coordinate transformation which will be discussed later. Accounting for the mass of element M in both its oxidized form, M_xO_y, and its un-oxidized form, M, by the principle mass conservation is useful in the discussion.

The current model can handle the oxidation of a single element, M, which undergoes the chemical oxidation reaction:

$$xM + \frac{y}{2}O_2 \longrightarrow M_xO_y. \tag{10}$$

Thus, for diffusion within a metallic alloy comprised of many elements, the oxidation of each element can only be considered separately. This presumes that only the element, M, despite the presence of other reactive elements, is uniquely reactive with the incoming diffusing oxygen.

In the model, the atoms of element M which undergo oxidation, $M_{total-R}$, are assumed to be located specifically within a certain width, $\Delta\lambda$, of the original metal alloy plane [6]. This assumption requires a homogeneous distribution of the atoms of element M within the original metal alloy layer as illustrated in Figure 4.
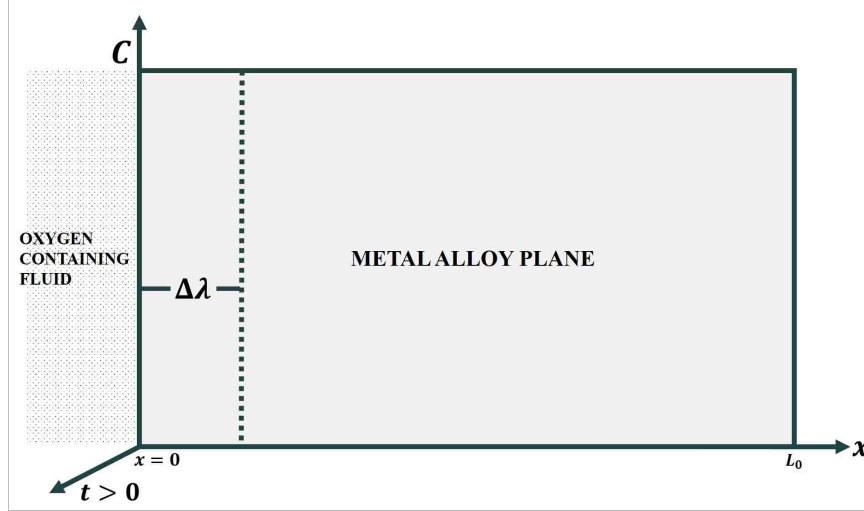
Figure 4: Width, $\Delta\lambda$, in Homogeneous Metal Plane

As the atomic oxygen diffuses into the plane, it reacts with M contained in $\Delta\lambda$ to form $M_{\mathrm{x}}O_{\mathrm{y}}$, which displaces M as shown in Figure 5. Although $\Delta\lambda$ shifts as oxidation proceeds, its width remains constant. Some atoms of element M diffuse into the formed oxide layer where they react with the diffusing oxygen. These atoms are denoted $M_{M_{\mathrm{x}}O_{\mathrm{y}}-R}$. Thus, two distinct reaction locations are identified in the present model: within the width $\Delta\lambda$ or within or on the surface of the oxide layer, $M_{\mathrm{x}}O_{\mathrm{y}}$. In terms of oxidation, what distinguishes these locations is the allocation of the M atoms originally reserved for oxidation within $\Delta\lambda$, denoted $M_{\Delta\lambda-R}$. In other words, a percentage of reacting M atoms originally located in $\Delta\lambda$ migrate into the oxide layer as seen in Figure 5.
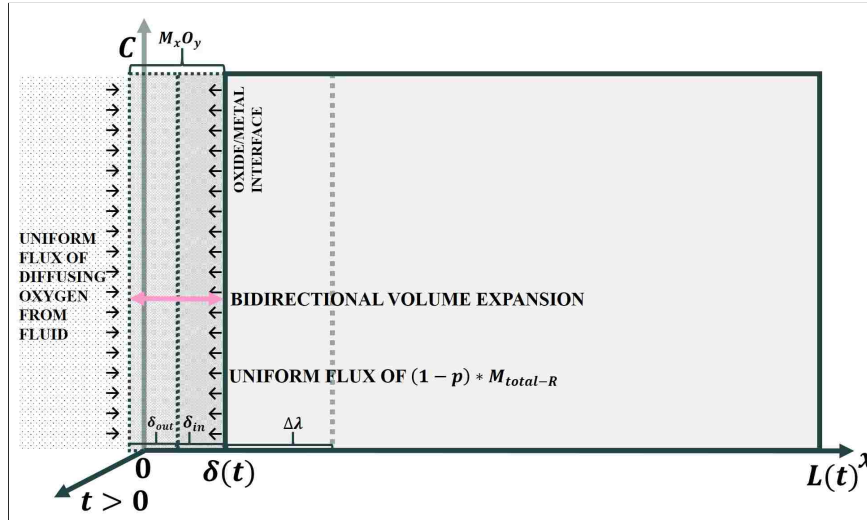
Figure 5: Oxidation Reaction Locations, $\Delta\lambda$ and $M_{\mathrm{x}}O_{\mathrm{y}}$, and δ_{in} and δ_{out}

Hereby, the parameter p is defined by the ratio:

$$p = \frac{M_{\Delta\lambda-R}}{M_{total-R}}. \tag{11}$$

Therefore, $1-p$ is

$$1 - p = \frac{M_{M_xO_y}}{M_{total-R}}. \tag{12}$$

If reacting M atoms tend to be oxidized within $\Delta\lambda$, the oxide layer exhibits compactness and higher density. Alternatively, a porous oxide layer is favored to the extent of M atoms migrating to and being oxidized within or on the surface the oxide layer [6]. To restate, the disparity in allocation of reacting M atoms leads to the formation of a compact inner oxide layer of thickness $\delta_{in}(t)$ as well as a porous outer layer of thickness $\delta_{out}(t)$ with respect to the x-direction as shown in Figure 5. To specify, the inner oxide layer partially forms via displacement of the reacting M atoms by the molecular product, M_xO_y. This displacement is accompanied by an inward inner layer volume expansion. The remnant non-reactive component metals of the alloy also comprise the inner oxide layer, resulting in its high density. The reaction occurring at the surface or within the formed oxide layer creates an outward outer layer volume expansion. This layer is assumed to be comprised of pure M_xO_y. This idea is supported by calculations done by Wagner, which indicate that the distribution of M atoms, or the cations in this case, in the oxide layer is not uniform [12].

At a time, $t + \Delta t$, the inner and outer layers change by $\Delta\delta_{in}$ and $\Delta\delta_{out}$, respectively. This is shown in Figure 6.
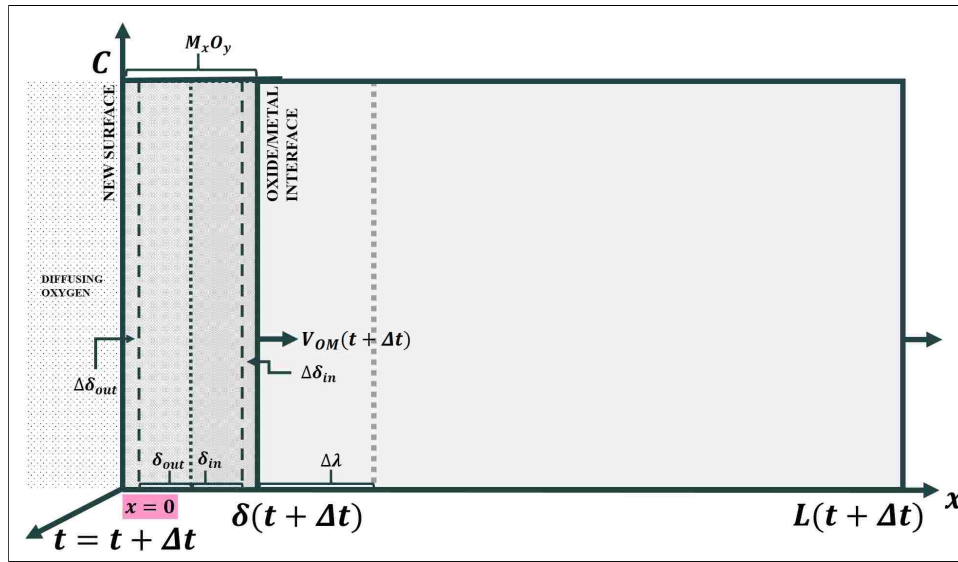
Figure 6: V_{OM} Obtained at $t + \Delta t$ by Fixing Calculating Coordinate at New Oxide Surface

Thus, the total change in thickness, $\Delta\delta_{tot}$, can be shown as

$$\Delta\delta_{tot} = \Delta\delta_{in} + \Delta\delta_{out}. \tag{13}$$

As suggested earlier, the volume expansion is assumed to occur bidirectionally: inward partially substituting the metal and outward beyond the spatial coordinate of the original surface of the metal as indicated in Figure 5. If the original point of the x-coordinate, $x = 0$, is continually calculated and fixed at the surface of the forming oxide layer, as illustrated in Figure 6, the velocity of the moving interface, V_{OM}, can be represented at time, $t + \Delta t$, by

$$V_{OM}(t + \Delta t) = \frac{\Delta\delta_{tot}}{\Delta t} = \frac{\Delta\delta_{in} + \Delta\delta_{out}}{\Delta t} \tag{14}$$

For the task of deriving $\Delta\delta_{in}$ and $\Delta\delta_{out}$ from the mass conservation of $M_{\Delta\lambda-R}$ and $M_{M_xO_y-R}$, respectively, relevant parameters are defined in addition to p and are compiled in Table 2. Essentially, the mass

Table 2: Parameters for Deriving V_{OM}

Parameter Symbol	Definition	Dimensions
ρ_{Me}	**Density of Metal Alloy**	$[\mathbf{M/L^3}]$
ρ_{in}	**Density of $\Delta\delta_{in}$**	$[\mathbf{M/L^3}]$
ρ_{out}	**Density of $\Delta\delta_{out}$**	$[\mathbf{M/L^3}]$
w	**Weight Ratio of Element M in Metal Alloy**	
r	**Mass Fraction of M in M_xO_y**	
p	$M_{\Delta\lambda-R}/M_{total-R}$	
$1-p$	$M_{M_xO_y-R}/M_{total-R}$	
$\Delta\lambda$	**Thickness of Layer in which $M_{total-R}$ are Located**	$[\mathbf{L}]$
K_r	**Scale Removal Rate**	$[\mathbf{L/t}]$

of the un-oxidized $M_{\Delta\lambda-R}$ per cross section of $\Delta\lambda$ is set equal to the mass of the oxidized $M_{\Delta\lambda-R}$ per cross section of $\Delta\delta_{in}$ as shown in (15) [6].

$$\rho_{Me}wp\Delta\lambda = r\rho_{in}\Delta\delta_{in} \tag{15}$$

Similarly, the mass of un-oxidized $M_{M_xO_y-R}$ per cross section of $\Delta\lambda$ is set equal to the mass of the sum of both oxidized and scaled off $M_{M_xO_y-R}$ per cross section of $\Delta\delta_{out}$ as expressed in equation (16). The scale removal of $\Delta\delta_{out}$ which is caused by erosion or ablation of the oxide layer is a function of conditions of fluid flow. For the present model, the scale removal rate, K_r is assigned a constant value, which will be described

14

later.

$$\rho_{Me}w(1-p)\Delta\lambda = r\rho_{out}\Delta\delta_{out} + r\rho_{out}K_r t \tag{16}$$

Solving equations (15) and (16) respectively for $\Delta\delta_{in}$ and $\Delta\delta_{out}$, substituting into equation (14), and simplifying yields

$$V_{OM}(t+\Delta t) = \frac{\rho_{Me}w\Delta\lambda}{r\cdot(t+\Delta t)}\left(\frac{p}{\rho_{in}} + \frac{1-p}{\rho_{out}}\right) + K_r. \tag{17}$$

At this point, a new factor, m, is defined as

$$m = \frac{\rho_{Me}w}{r}\left(\frac{p}{\rho_{in}} + \frac{1-p}{\rho_{out}}\right), \tag{18}$$

such that equation (17) can be expressed as

$$V_{OM}(t+\Delta t) = \frac{m\Delta\lambda}{t+\Delta t} + K_r. \tag{19}$$

In redefining V_{Me}, first equating the displacement of L to displacement of the oxide layer at time $t+\Delta t$ with respect to $\Delta\lambda$ gives

$$L(t+\Delta t) - L_0 = \Delta\delta_{tot}(t+\Delta t) - \Delta\lambda \tag{20}$$

whereby equation (2) becomes

$$V_{Me}(t+\Delta t) = \frac{\Delta\delta_{tot}(t+\Delta t) - \Delta\lambda}{t+\Delta t}. \tag{21}$$

By substitution of equations (14) and (19) into equation(21), the task of expressing V_{Me} in terms of V_{OM} is complete by equation (22).

$$V_{Me}(t+\Delta t) = \left(1 - \frac{1}{m}\right)V_{OM}(t+\Delta t) - \frac{K_r}{m} \tag{22}$$

The governing equations are rewritten in terms of V_{OM}. Subsequently, non-dimensionalization is performed first for the advection-diffusion equation, then for Fick's second law, and finally for the interface condition. The procedure for non-dimensionalizing the advection-diffusion equation is given in Appendix A. The results of the preceding operations are tabulated in Table 3.

Table 3: Non-Dimensionalized Governing Equations for Planar Diffusion Model for Oxidation

Phase	Oxide Layer	Metal Layer		Interface
Equation Name	Fick's Second Law	Advection-Diffusion		Interface Condition
Governing Equations ($\bar{t} > 0$)	$\frac{D_{Me}}{D_{Ox}}\frac{\partial \bar{C}_1(\bar{x},\bar{t})}{\partial \bar{t}} = \frac{\partial^2 \bar{C}_1(\bar{x},\bar{t})}{\partial \bar{x}^2}$	$\frac{\partial \bar{C}_2(\bar{x},\bar{t})}{\partial \bar{t}} = \frac{\partial^2 \bar{C}_2(\bar{x},\bar{t})}{\partial \bar{x}^2} - \left(\left(1-\frac{1}{m}\right)\bar{V}_{OM}(\bar{t}) - \frac{\bar{K}_r}{m}\right)\frac{\partial \bar{C}_2(\bar{x},\bar{t})}{\partial \bar{x}}$		$\frac{\frac{D_{Ox}}{D_{Me}}\frac{\partial \bar{C}_1(\bar{\delta}(\bar{t}),\bar{t})}{\partial \bar{x}} - \frac{\partial \bar{C}_2(\bar{\delta}(\bar{t}),\bar{t})}{\partial \bar{x}}}{|\bar{C}_{MO} - \bar{C}_{OM}|} = \bar{V}_{OM}(\bar{t})$
$\bar{x}$-domain	$0 < \bar{x} < \bar{\delta}(\bar{t})$	$\bar{\delta}(\bar{t}) < \bar{x} < \bar{L}(\bar{t})$		
Boundary Conditions	$\bar{C}_1(0,t) = 1$ $\bar{C}_1(\bar{\delta}(\bar{t}),\bar{t}) = \bar{C}_{OM}$	$\bar{C}_2(\bar{\delta}(\bar{t}),\bar{t}) = \bar{C}_{MO}$ $\bar{C}_2(\bar{L}(\bar{t})) = \bar{C}_{M\infty}$		
Initial Condition	$\bar{C}_1(\bar{x},0) = 0$; $0 < \bar{x} < \infty$	$\bar{C}_2(\bar{x},0) = 0$; $0 < \bar{x} < \infty$		$\delta(0) = 0$
Dimensionless Variables				
$\bar{t} = \frac{D_{Me}t}{(L_0)^2}$	$\bar{C}_2 = \frac{C_2}{C_{O0}}$	$\bar{x} = \frac{x}{L_0}$		$\bar{L}(\bar{t}) = \frac{L(t)}{L_0}$
$\bar{C}_1 = \frac{C_1}{C_{O0}}$	$\bar{K}_r = \frac{K_r L_0}{D_{Me}}$	$\bar{\delta}(\bar{t}) = \frac{\delta(t)}{L_0}$		$\bar{V}_{OM}(\bar{t}) = \frac{V_{OM}(t)L_0}{D_{Me}}$
$\bar{C}_{OM} = \frac{C_{OM}}{C_{O0}}$	$\bar{C}_{MO} = \frac{C_{MO}}{C_{O0}}$	$\bar{C}_{M\infty} = \frac{C_{M\infty}}{C_{O0}}$		

2.4 Coordinate Transformation

Next, the application of a coordinate transformation in non-dimensionalized spatial direction $\bar{x}$ to governing equations is discussed. This transformation is inspired by the Landau position transformation, which is characterized by fixed spatial boundaries [15]. Behavior of a moving boundary is explicitly captured when it is immobilized via a transformation of coordinate. In the present model, the two non-dimensional physical moving boundaries are identified as $\bar{\delta}(\bar{t})$ and $\bar{L}(\bar{t})$. The former represents the oxide/metal interface which travels with non-dimesional velocity, $\bar{V}_{OM}(\bar{t})$. The latter stands for the side of the metal alloy which is unexposed to the oxidizing fluid and moves with non-dimensinal velocity, $\bar{V}_{Me}(\bar{t})$. In the present model, the task of immobilizing of $\bar{L}(\bar{t})$ is achieved while the procession of $\bar{\delta}(\bar{t})$ is tracked. This task naturally follows from the procedure for non-dimensionalization of the governing equations, wherein $\bar{V}_{Me}$, which represents the advection velocity, is eliminated. Ultimately, a non-linear boundary value problem which does not explicitly consider advection is mathematically created for a fixed domain. The coordinate transformation procedure is outlined. The transformation of the spatial coordinate is carried out first for the domain of the metal phase and then for that of the oxide phase. The transformed coordinate is then extended to the governing equations. The interface condition is described as well.

The transformation of $\bar{x}$-coordinate in the advection-diffusion region (metal phase) starts with identifying the $\bar{x}$ domain:

$$\bar{\delta}(\bar{t}) < \bar{x} < \bar{L}(\bar{t}). \tag{23}$$

The transformed coordinate is represented by $\bar{y}$. In order to fix the upper bound of the $\bar{x}$ domain to 1 such

that,

$$\bar{y}((\bar{x} = \bar{L}(\bar{t})) = 1), \tag{24}$$

a relation between $\bar{L}(\bar{t})$ and 1 is sought. Recall the the non-dimensional form of equation (2) is

$$\bar{V}_{Me}(\bar{t}) = \frac{\bar{L}(\bar{t}) - 1}{\bar{t}}. \tag{25}$$

Solving for 1 with $\bar{V}_{Me}(\bar{t})$ in terms of $\bar{V}_{OM}(\bar{t})$ gives

$$1 = \frac{\bar{K}_r\bar{t}}{m} - \left(1 - \frac{1}{m}\right)\bar{V}_{OM}(\bar{t}) \cdot \bar{t} + \bar{L}(\bar{t}). \tag{26}$$

The non-dimensional forms of equations (7) and (9) respectively give

$$\bar{V}_{OM}(\bar{t}) \cdot \bar{t} = \bar{\delta}(\bar{t}). \tag{27}$$

Substitution of equation (27) into equation (26) gives

$$1 = \frac{\bar{K}_r\bar{t}}{m} - \left(1 - \frac{1}{m}\right)\bar{\delta}(\bar{t}) + \bar{L}(\bar{t}). \tag{28}$$

Substitution of equation (28) into equation (23) gives

$$\frac{\bar{\delta}(\bar{t}) + \bar{K}_r\bar{t}}{m} < \bar{x} + \frac{1}{m}((1-m)\bar{\delta}(\bar{t}) + \bar{K}_r\bar{t}) < 1. \tag{29}$$

Thus, the expression for transformed coordinate $\bar{y}$ in the advection-diffusion region is

$$\bar{y} = \bar{x} + \frac{1}{m}((1-m)\bar{\delta}(\bar{t}) + \bar{K}_r\bar{t}), \quad for \quad \bar{\delta}(\bar{t}) < \bar{x} < \bar{L}(\bar{t}), \quad \frac{\bar{\delta}(\bar{t}) + \bar{K}_r\bar{t}}{m} < \bar{y} < 1. \tag{30}$$

The transformation of $\bar{x}$-coordinate in the Fick's second law of diffusion region (oxide phase) starts with identifying the $\bar{x}$ domain:

$$0 < \bar{x} < \bar{\delta}(\bar{t}). \tag{31}$$

The $\bar{y}$-coordinate at the interface in both the domains of the advection-diffusion region and the Fick's second law of diffusion region is equated by equation (32):

$$\bar{y}(\bar{x} = \bar{\delta}^-(\bar{t})) = \bar{y}(\bar{x} = \bar{\delta}^+(\bar{t})) = \frac{\bar{\delta}(\bar{t}) + \bar{K}_r\bar{t}}{m}. \tag{32}$$

Substitution of equation (32) into equation (31) yields

$$\frac{\bar{K}_r\bar{t}}{m} < \frac{\bar{x} + \bar{K}_r\bar{t}}{m} < \frac{\bar{\delta}(\bar{t}) + \bar{K}_r\bar{t}}{m}. \tag{33}$$

Noting that in $0 < \bar{x} < \bar{\delta}(\bar{t})$

$$\bar{t} = \frac{\bar{x}}{\bar{V}_{OM}(\bar{t})}, \tag{34}$$

the expression in equation (33) changes to

$$0 < \frac{\bar{x}}{\bar{m}}\left(1 + \frac{\bar{K}_r}{\bar{V}_{OM}(\bar{t})}\right) < \frac{\bar{\delta}(\bar{t}) + \bar{K}_r\bar{t}}{m}. \tag{35}$$

Thus, expression for transformed coordinate $\bar{y}$ is

$$\bar{y} = \frac{\bar{x}}{\bar{m}}\left(1 + \frac{\bar{K}_r}{\bar{V}_{OM}(\bar{t})}\right) \quad for \quad 0 < \bar{x} < \bar{\delta}(\bar{t}), \quad 0 < \bar{y} < \frac{\bar{\delta}(\bar{t}) + \bar{K}_r\bar{t}}{m}. \tag{36}$$

Now, the transformed coordinate is applied to the non-dimensional governing equations. For the advection-diffusion region, the governing equation is

$$\frac{\partial \bar{C}_2(\bar{x},\bar{t})}{\partial \bar{t}} = \frac{\partial^2 \bar{C}_2(\bar{x},\bar{t})}{\partial \bar{x}^2} - \left(\left(1 - \frac{1}{m}\right)\bar{V}_{OM}(\bar{t}) - \frac{\bar{K}_r}{m}\right)\frac{\partial \bar{C}_2(\bar{x},\bar{t})}{\partial \bar{x}}. \tag{37}$$

The transformed coordinate from equation (30) is rewritten in equation (38) with the non-dimensional oxygen concentration, $\bar{C}_2$, which is a function of time and position of both the non-transformed and transformed coordinate.

$$\bar{y} = \bar{x} + \frac{1}{m}((1-m)\bar{\delta}(\bar{t}) + \bar{K}_r\bar{t}); \quad \bar{C}_2(\bar{x},\bar{t}) = \bar{C}_2(\bar{y},\bar{t}). \tag{38}$$

Application of the chain rule to equation (38) gives

$$\frac{\partial \bar{C}_2(\bar{x},\bar{t})}{\partial \bar{t}} = \frac{\partial \bar{C}_2(\bar{y},\bar{t})}{\partial \bar{y}}\left(\frac{1}{m}((1-m)\bar{V}_{OM}(\bar{t}) + \bar{K}_r\bar{t}\right) + \frac{\partial \bar{C}_2(\bar{y},\bar{t})}{\partial \bar{t}}, \tag{39}$$

$$\frac{\partial \bar{C}_2(\bar{x},\bar{t})}{\partial \bar{x}} = \frac{\partial \bar{C}_2(\bar{y},\bar{t})}{\partial \bar{y}}, \tag{40}$$

and

$$\frac{\partial^2 \bar{C}_2(\bar{x},\bar{t})}{\partial \bar{x}^2} = \frac{\partial^2 \bar{C}_2(\bar{y},\bar{t})}{\partial \bar{y}^2}. \tag{41}$$

18

Substituting equations (39), (40), and (41) into equation (37) gives

$$\frac{\partial \bar{C}_2(\bar{y}, \bar{t})}{\partial \bar{t}} = \frac{\partial^2 \bar{C}_2(\bar{y}, \bar{t})}{\partial \bar{y}^2} \tag{42}$$

which is the transformed advection–diffusion equation. For the Fick's second law of diffusion region, the governing equation is

$$\frac{D_{Me}}{D_{Ox}} \frac{\partial \bar{C}_1(\bar{x}, \bar{t})}{\partial \bar{t}} = \frac{\partial^2 \bar{C}_1(\bar{x}, \bar{t})}{\partial \bar{x}^2}. \tag{43}$$

The transformed coordinate from equation (36) is rewritten in equation (44) with the non-dimensional oxygen concentration, $\bar{C}_1$:

$$\bar{y} = \frac{\bar{x}}{\bar{m}} \left(1 + \frac{\bar{K}_r}{\bar{V}_{OM}(\bar{t})} \right); \quad \bar{C}_1(\bar{x}, \bar{t}) = \bar{C}_1(\bar{y}, \bar{t}). \tag{44}$$

Application of chain rule to equation (44) gives

$$\frac{\partial \bar{C}_1(\bar{x}, \bar{t})}{\partial \bar{t}} = \frac{\partial \bar{C}_1(\bar{y}, \bar{t})}{\partial \bar{t}}, \tag{45}$$

$$\frac{\partial \bar{C}_1(\bar{x}, \bar{t})}{\partial \bar{x}} = \frac{\partial \bar{C}_1(\bar{y}, \bar{t})}{\partial \bar{y}} \left(\frac{1}{m} \left(1 + \frac{\bar{K}_r}{\bar{V}_{OM}(\bar{t})} \right) \right), \tag{46}$$

and

$$\frac{\partial^2 \bar{C}_1(\bar{x}, \bar{t})}{\partial \bar{x}^2} = \frac{\partial^2 \bar{C}_2(\bar{y}, \bar{t})}{\partial \bar{y}^2} \left(\frac{1}{m} \left(1 + \frac{\bar{K}_r}{\bar{V}_{OM}(\bar{t})} \right) \right)^2. \tag{47}$$

Substituting equations (45), (46), and (47) into equation (43) gives

$$\frac{D_{Me}}{D_{Ox}} \left(\frac{\partial \bar{C}_1(\bar{y}, \bar{t})}{\partial \bar{t}} \right) = \left(\frac{1}{m} \left(1 + \frac{\bar{K}_r}{\bar{V}_{OM}(\bar{t})} \right) \right)^2 \frac{\partial^2 \bar{C}_1(\bar{y}, \bar{t})}{\partial \bar{y}^2}. \tag{48}$$

which is the transformed Fick's second law of diffusion. The results of the coordinate transformation so far are summarized in Table 4. The fixed domain of the planar model is illustrated in Figure 7.

Table 4: Transformed Partial Differential Equations for Planar Diffusion Model on Fixed Domain

Phase	Oxide Layer	Metal Layer
Equation Name **Transformed Coordinate,** $\bar{y}$	**Fick's Second Law Region** $\bar{y} = \frac{\bar{x}}{m}\left(1 + \frac{\bar{K}_r}{\bar{V}_{OM}(\bar{t})}\right)$ $\quad for \quad 0 < \bar{x} < \bar{\delta}(\bar{t})$	**Advection-Diffusion Region** $\bar{y} = \bar{x} + \frac{1}{m}((1-m)\bar{\delta}(\bar{t}) + \bar{K}_r\bar{t}), \quad for \quad \bar{\delta}(\bar{t}) < \bar{x} < \bar{L}(\bar{t})$
Governing Equations $(\bar{t} > 0)$	$\frac{D_{Me}}{D_{Ox}}\left(\frac{\partial \bar{C}_1(\bar{y},\bar{t})}{\partial t}\right) = \left(\frac{1}{m}\left(1 + \frac{\bar{K}_r}{\bar{V}_{OM}(\bar{t})}\right)\right)^2 \frac{\partial^2 \bar{C}_1(\bar{y},\bar{t})}{\partial \bar{y}^2}$	$\frac{\partial \bar{C}_2(\bar{y},\bar{t})}{\partial t} = \frac{\partial^2 \bar{C}_2(\bar{y},\bar{t})}{\partial \bar{y}^2}$
$\bar{y}$-**domain**	$0 < \bar{y} < \frac{\bar{\delta}(\bar{t}) + \bar{K}_r\bar{t}}{m}$	$\frac{\bar{\delta}(\bar{t}) + \bar{K}_r\bar{t}}{m} < \bar{y} < 1$
Boundary Conditions	$\bar{C}_1(0,\bar{t}) = 1$ $\bar{C}_1\left(\frac{\bar{\delta}^-(\bar{t}) + \bar{K}_r\bar{t}}{m},\bar{t}\right) = \bar{C}_{OM}$	$\bar{C}_2\left(\frac{\bar{\delta}^+(\bar{t}) + \bar{K}_r\bar{t}}{m},\bar{t}\right) = \bar{C}_{MO}$ $\bar{C}_2(1,\bar{t}) = \bar{C}_{M\infty}$
Initial Condition	$\bar{C}_1(\bar{y},0) = 0;\ 0 < \bar{y} < 1$	$\bar{C}_2(\bar{y},0) = 0;\ 0 < \bar{y} < 1$
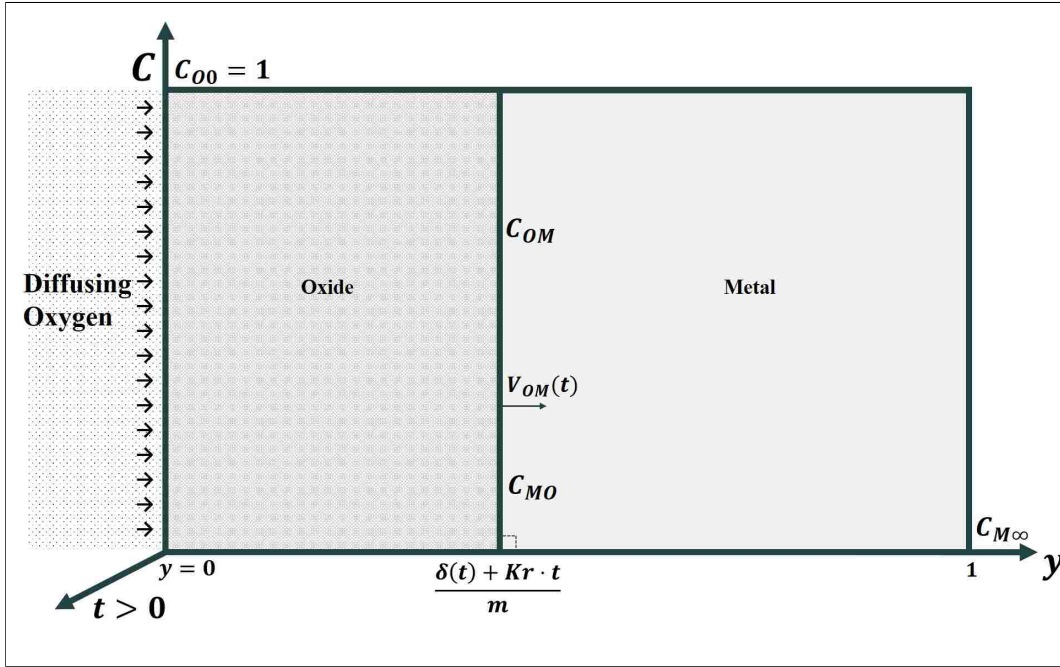
Figure 7: Width, $\Delta\lambda$, and Homogeneous Distribution of M Atoms in Metal Plane

2.5 Simplification of Diffusion Coefficient

At this point, the transformation is normally applied to the interface condition, which is in turn substituted into the two transformed partial differential equations for further simplification and closure. In the present model, the two transformed equations are instead simplified in the following manner such that transforming the interface condition is avoided [17]. First, a modification of the diffusion coefficients results in

$$\bar{D}_{Ox} = \frac{D_{Ox}}{D_{me}}\left(\frac{1}{m}\left(1 + \frac{\bar{K}_r}{\bar{V}_{OM}(\bar{t})}\right)\right)^2, \quad \bar{D}_{Me} = 1 \tag{49}$$

which allows for the transformed equations to be of the form

$$\frac{\partial \bar{C}(\bar{y}, \bar{t})}{\partial \bar{t}} = \bar{D}(\bar{C}(\bar{y}, \bar{t})) \frac{\partial^2 \bar{C}(\bar{y}, \bar{t})}{\partial \bar{y}^2}. \tag{50}$$

in which $\bar{D}$ and $\bar{C}$ assume the associated values in equation (49) and in Table 4, respectively. Keeping the goal of simplification in mind, it is necessary to describe how the diffusion coefficient behaves as a function of oxygen concentration. Physical values of oxygen concentration, $\bar{C}$, exhibit a break in continuity at the interval $[\bar{C}_{MO}, \bar{C}_{OM}]$ where the diffusion coeffecent, $\bar{D}$, is undefined. Thus, equation (50) is only valid in regions outside this interval. To reconcile this issue, the values of $\bar{D}$ on $[\bar{C}_{MO}, \bar{C}_{OM}]$ are set equal to zero as shown in Figure 8. By doing so, the values of $\bar{C}$ are no longer restricted in equation (50). Thus, the transformation of the interface condition is eliminated.
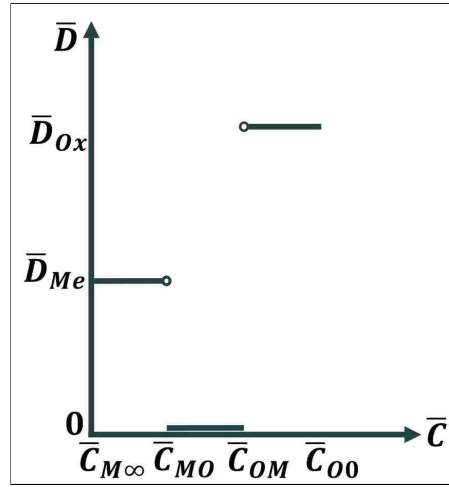
Figure 8: Diffusion Coefficient, $\bar{D}$, as Discontinuous Function of Oxygen Concentration, $\bar{C}$

The justification for this simplification is explained by the steep decrease in oxygen concentration from $\bar{C}_{OM}$ to $\bar{C}_{MO}$ within a boundary layer of a thin thickness. This steep decrease is modeled as a finite jump when the thickness is reduced to a zero thickness through which diffusion is impossible. The new governing equation for all phases of the planar oxidation model is summarized in Table 5.

Table 5: Simplified Planar Diffusion Governing Equation

Governing Equation	$\frac{\partial \bar{C}(\bar{y},\bar{t})}{\partial \bar{t}} = \bar{D}(\bar{C}(\bar{y},\bar{t}))\frac{\partial^2 \bar{C}(\bar{y},\bar{t})}{\partial \bar{y}^2}$
Diffusion Coefficient, $\bar{D}(\bar{C}(\bar{y},\bar{t}))$	$\bar{D} = \bar{D}_{Ox}$ **on** $[1,\bar{C}_{OM})$ $\bar{D} = 0$ **on** $[\bar{C}_{OM},\bar{C}_{MO}]$ $\bar{D} = \bar{D}_{Me}$ **on** $(\bar{C}_{MO},\bar{C}_{M\infty}]$
Boundary Conditions	$\bar{C}(0,\bar{t}) = 1$ $\bar{C}(1,\bar{t}) = \bar{C}_{M\infty}$
Initial Condition	$\bar{C}(\bar{y},0) = 0$ **on** $0 < \bar{y} < 1$

2.6 Kirchhoff Transformation

For anticipated numerical simulation, further simplification is achieved by applying the Kirchhoff transformation to the governing equation shown in Table 5 [19]. Noting that the diffusion coefficient, $\bar{D}$, is concentration dependent as in equation (51),

$$\bar{D} = \bar{D}(\bar{C}(\bar{y},\bar{t})), \tag{51}$$

a new variable Z is defined by

$$\frac{\partial Z(\bar{C}(\bar{y},\bar{t}))}{\partial \bar{C}} = \bar{D}(\bar{C}(\bar{y},\bar{t})). \tag{52}$$

Hereby, the discontinuous relationship between the diffusion coefficient and oxygen concentration, seen in Figure 8, is removed as seen in Figure 9. The region where Z is constant represents the latent change in molar atomic oxygen concentration, $\bar{C}$, across the phase boundary which relates to what drives phase change. Application of the chain rule to equation (52) and substitution of the result into equation (50) in dimensionless form gives

$$\frac{\partial \bar{C}(\bar{y},\bar{t})}{\partial \bar{t}} = \frac{\partial^2 \bar{Z}(\bar{C}(\bar{y},\bar{t}))}{\partial \bar{y}^2}. \tag{53}$$
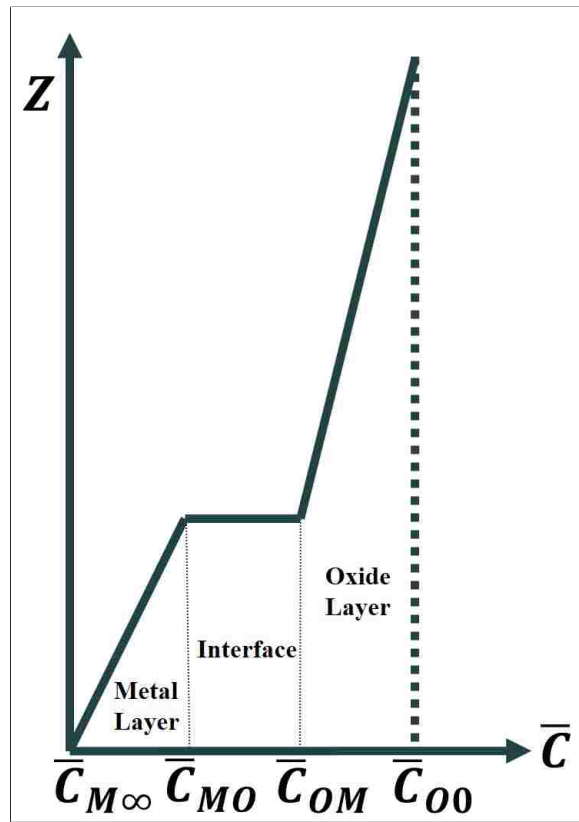
Figure 9: Function $Z(\bar{C})$ from Kirchhoff Transformation

Chapter 3 Numerical Method

3.1 Implicit Scheme

An implicit finite difference method typically used for phase change moving boundary problems called the "enthalpy method" is implemented [20]. This numerical method results in a set of non-linear equations and is applied to a fixed grid. The spatial interval $[0, a]$ is divided into N nodes of equal width, $\Delta \bar{y}$, with the end nodes of width $\dfrac{\Delta \bar{y}}{2}$. The index for time and space are n and i, respectively. From this point, the overbar is removed as all terms will be considered non-dimensional. In a center-in-space scheme, for interior node i to advance from time level n to $n+1$ through time step Δt, equation (53) can be expressed implicitly by

$$\frac{C_i^{n+1} - C_i^n}{\Delta t} = \frac{1}{\Delta y^2}[Z(C_{i+1}^{n+1}) - 2Z(C_i^{n+1}) + Z(C_{i-1}^{n+1})]. \tag{54}$$

The value of C is specified to be 1 at the exposed surface and $C_{M\infty}$ at the metal front. These boundary conditions are expressed by

$$C_1^{n+1} = 1 \tag{55}$$

and

$$C_N^{n+1} = C_{M\infty}. \tag{56}$$

3.2 Application of Newton-Raphson Method

Thus, equations (54), (55), and (56) are the system of non-linear equations for $C_i^{n+1} = 1, \ldots, N$. The iterative scheme applied is the Newton-Raphson method for which a new iterative index, k, is introduced whereby equation (54) can be expressed as

$$
\begin{aligned}
\frac{C_{i,n+1}^{k+1} - C_{i,n+1}^1}{\Delta t} = \; & \frac{1}{\Delta y^2}[Z(C_{i+1,n+1}^k) + D(C_{i+1,n+1}^k)(C_{i+1,n+1}^{k+1} - C_{i+1,n+1}^k)] \quad - \\
& \frac{2}{\Delta y^2}[Z(C_{i,n+1}^k) + D(C_{i,n+1}^k)(C_{i,n+1}^{k+1} - C_{i,n+1}^k)] \quad + \\
& \frac{1}{\Delta y^2}[Z(C_{i-1,n+1}^k) + D(C_{i-1,n+1}^k)(C_{i-1,n+1}^{k+1} - C_{i-1,n+1}^k)],
\end{aligned}
\tag{57}
$$

in which two substitutions are made. The first, an approximation from the first order Taylor Series expansion, is

$$Z(C_j^{n+1}) = Z(C_{j,n+1}^k) + D(C_{j,n+1}^k)(C_{j,n+1}^{k+1} - C_{j,n+1}^k), \tag{58}$$

and the second is

$$C_i^n = C_{i,n+1}^1.$$ (59)

3.3 Tri-Diagonal Matrix Algorithm

Coefficients of $C_{j,n+1}^{k+1}$ for a tri-diagonal matrix formed from a system of linear equations are determined from equation (57). For the interior nodes i belonging to $[2, N-1]$, the coefficients, given symbols f, g, and h, are expressed in Table 6.

Table 6: Coefficients of $C_{j,n+1}^{k+1}$ for Tri-Diagonal Matrix

Symbol	Spatial Node, j	Discretized Concentration, C	Coefficient
f	$i-1$	$C_{i-1,n+1}^{k+1}$	$-\dfrac{1}{\Delta y^2}(D(C_{i-1,n+1}^k))$
g	i	$C_{i,n+1}^{k+1}$	$\dfrac{2}{\Delta y^2}(D(C_{i,n+1}^k)) + \dfrac{1}{\Delta t}$
h	$i+1$	$C_{i+1,n+1}^{k+1}$	$-\dfrac{1}{\Delta y^2}(D(C_{i+1,n+1}^k))$

The matrix equation is depicted in equation (60) and is solved for oxygen concentration, $C_{j,n+1}^{k+1}$, with a tri-diagonal matrix algorithm.

$$
\begin{pmatrix}
g & h & \cdots & 0 \\
f & \ddots & \ddots & \vdots \\
\vdots & \ddots & \ddots & h \\
0 & \cdots & f & g
\end{pmatrix}
\begin{pmatrix}
C_1^{k+1} \\
C_2^{k+1} \\
\vdots \\
C_N^{k+1}
\end{pmatrix}
=
\begin{pmatrix}
Q(C_1^k) \\
Q(C_2^k) \\
\vdots \\
Q(C_N^k)
\end{pmatrix}
$$ (60)

The function $Q(C_j^k)$ on the right hand side of equation (60) is given by

$$
\begin{aligned}
Q(C_j^k) = C_{i,n+1}^1 + \frac{1}{\Delta y^2}[&Z(C_{i-1,n+1}^k) - 2Z(C_{i,n+1}^k) + Z(C_{i+1,n+1}^k) \quad - \\
&D(C_{i-1,n+1}^k)(C_{i-1,n+1}^k) + 2D(C_{i,n+1}^k)(C_{i,n+1}^k) \quad - \\
&D(C_{i+1,n+1}^k)(C_{i+1,n+1}^k)].
\end{aligned}
$$ (61)

The iteration begins with (59) and proceeds until

$$max \left| \frac{C_{i,n+1}^{k+1} - C_{i,n+1}^k}{C_{i,n+1}^k} \right| \leq \epsilon, \quad i = 1, \ldots, N,$$ (62)

in which ϵ is a small number [17].

Recalling from equation (49) that the diffusion coefficient, D, is a function of V_{OM}, and thus a function of t, the numerical code is designed to calculate V_{OM} at each time step [6].

The algorithm of the numerical code is designed to obtain a fixed advance of the nominal interface position $\Delta\delta^{nom}$ at each time step. It is described as follows:

1. The advance of the interface position, $\Delta\delta^k$, is compared with the nominal interface position, $\Delta\delta^{nom}$; if the discrepancy is larger than a given percentage, the results are discarded.

2. After each time step, Δt^k, the interface velocity, V_{OM}^k is calculated from the new interface position, $\Delta\delta^k$, by

$$V_{OM}^k = \frac{\Delta\delta^k}{\Delta t^k}. \tag{63}$$

3. The new interface velocity, V_{OM}^{k+1} is extrapolated with respect to the next new interface position, $\Delta\delta^{k+1}$, by

$$V_{OM}^{k+1} = \frac{\Delta\delta^{k+1}}{\Delta\delta^k} V_{OM}^k. \tag{64}$$

4. Thus, the new time step, Δt^{k+1}, is calculated by

$$\Delta t^{k+1} = \frac{\Delta\delta^{k+1}}{V_{OM}^{k+1}}. \tag{65}$$

5. The iterative procedure continues until the selected time step produces and interface advance within the specified tolerance relative to the nominal value.

The numerical code was compiled using Microsoft Visual C++ Studio.

Chapter 4 Numerical Simulation

The present oxidation model is used to simulate oxidation conditions in nuclear reactor coolant environments. From certain aspects of the coolant environment, the parameters needed for the oxidation model are obtained. The first aspect is the type of structural material, in this case a stainless steel alloy, used in the containment design. From this information alone, the weight ratios, w, of the component metals, the density of the metal alloy, ρ_{Me}, and the solubility limit concentration of oxygen in the metal layer, C_{MO}, are determined. The next two aspects are the temperature and oxygen concentration of the contained liquid coolant. From these aspects, the stoichiometry of the possible metal oxides is predicted. This provides ρ_{in} and ρ_{out}, the inner and outer oxide layer densities for each oxide, and the mass fraction, r, of the metal M in its corresponding oxide, M_xO_y. Additionally, this information provides the diffusivity of oxygen in the metal alloy layer, D_{Me}, the minimum concentration of oxygen needed to form of the inner oxide layer, C_{OM} and D_{Ox}, the diffusivity of oxygen in the oxide layer. The remaining parameter needed is the scale removal rate, K_r, which depends on the preceding three aspects and also on the velocity of the moving liquid coolant [1]. To summarize, the four aspects considered for the present oxidation simulation are: the type of stainless steel alloy, the liquid coolant temperature, the oxygen concentration of the coolant, and the liquid coolant velocity.

These four aspects were taken into account as control variables in corrosion experiments done by Zhang [1]. Hereby, simulation of these experimental conditions is ideal for two reasons. The first is, as mentioned, the input parameters for the model are obtained from a single controlled experiment in a nuclear coolant system environment. The second is that the experimental results are used as a benchmark for the numerical simulation. Each aspect of the experiments is discussed in relation to how the necessary parameters are derived.

4.1 Selection of EP-823 Stainless Steel Alloy

In the experiments, a variety of steels had been subject to typical operating conditions of nuclear reactor coolant environments. The oxide layer growth of each type of steel was monitored. The resulting experimental thickness of the oxide layer, δ, was extrapolated to its steady state, or asymptotic, thickness, δ_s. The typical spallation thickness for stainless steel, or the minimum thickness at which the oxide layer is no longer stable in this environment, had been approximated to and accepted as 40 µm [1]. Based on the experimental results, the steel which exhibited formidable resistance to liquid metal coolant corrosion and oxidation was found to be EP-823 stainless steel alloy. In experimental conditions, the stable and protective oxide layer formed via oxidation of EP-823 alloy was predicted to reach its steady state thickness of 35.8 µm over a period of 26 years, which is below the typical spallation thickness [1]. Because this metal alloy had demonstrated

promise as a structural material based on the experimental results, its oxidation is characterized in the present model.

4.2 Derivation of Simulation Parameters

4.2.1 Weight Ratios of Alloying Elements

The weight ratios, w, of the component elements of EP-823 are shown in Table 7 [21]. The term 'weight ratio' is the mass of the alloying element in a given total mass of alloy to the given total mass.

Table 7: Chemical Composition of Martensitic Stainless Steel Alloy EP-823

Element	Sulfur	Boron	Phosphorus	Copper	Aluminum	Cerium	Carbon	Niobium	Vanadium	Manganese	Tungsten	Nickel	Molybdenum	Silicon	Chromium	Iron
Symbol	S	B	P	Cu	Al	Ce	C	Nb	V	Mn	W	Ni	Mo	Si	Cr	Fe
Weight Ratio	0.00004	0.00005	0.00005	0.0001	0.0002	0.0008	0.0017	0.0026	0.0034	0.0054	0.006	0.0065	0.007	0.0111	0.1169	0.84

4.2.2 Mass Fraction of M in M_xO_y

In the corrosion experiments on EP-823 alloy performed by Zhang [1], temperature, oxygen concentration, and velocity of the coolant, in this case Lead-bismuth eutectic (LBE), were controlled at $743\,\mathrm{K}$, $0.01\,\mathrm{ppm}$, and $1.9\,\mathrm{m\,s^{-1}}$, respectively. As mentioned, this information is used in identifying possible metal oxides using the Ellingham diagram, a graphical representation of the stability of metal oxides [22]. This process involves first selecting only the metal alloying components of EP-823. Thus, non-metal elements included in Table 7 are removed. An updated list is shown in Table 8. Although silicon is not a metal, it is included in this list.

Table 8: Alloying Elements of EP-823 Considered for Oxidation Model

Element	Copper	Aluminum	Cerium	Niobium	Vanadium	Manganese	Tungsten	Nickel	Molybdenum	Silicon	Chromium	Iron
Symbol	Cu	Al	Ce	Nb	V	Mn	W	Ni	Mo	Si	Cr	Fe
Weight Ratio	0.0001	0.0002	0.0008	0.0026	0.0034	0.0054	0.006	0.0065	0.007	0.0111	0.1169	0.84

To read the Ellingham diagram, the partial pressure of diatomic oxygen in LBE, P_{O_2}, is needed. Equation (66), is derived from the free energy values of the dissociation of diatomic oxygen in LBE, $\frac{1}{2}O_2(g) \longrightarrow O$.

$$\log P_{O_2} = 2\log(\mathrm{wt\text{-}\%O}) + 2\log\left(\frac{208}{16}\right) + \frac{2}{2.3R}\left(\frac{-12398}{T} + 27.938\right). \tag{66}$$

This relates the atomic oxygen concentration in LBE, $0.01\,\mathrm{ppm}$ or $1 \times 10^{-6}\,\mathrm{wt.\text{-}\%O}$ and absolute temperature T, in Kelvin, to P_{O_2} in atmospheres [23]. P_{O_2} is calculated to be $5.1 \times 10^{-17}\,\mathrm{atm}$.

Figure 10 shows the Ellingham diagram obtained from [24]. A series of free energy of formation lines for oxidation reactions is intercepted by the experimental temperature, $743\,\mathrm{K}$ or $470\,^\circ\mathrm{C}$. This point of intersection on each formation line corresponding to elements in Table 8 is again crossed by a second line

linking the temperature and the formation reaction to its equilibrium partial pressure. Those reactions which show an equilibrium partial pressure below that of the experimental partial pressure, P_{O_2}, are highlighted. The relatively low equilibrium partial pressure favors oxidation, rather than reduction. The oxides resulting from these reactions are listed.
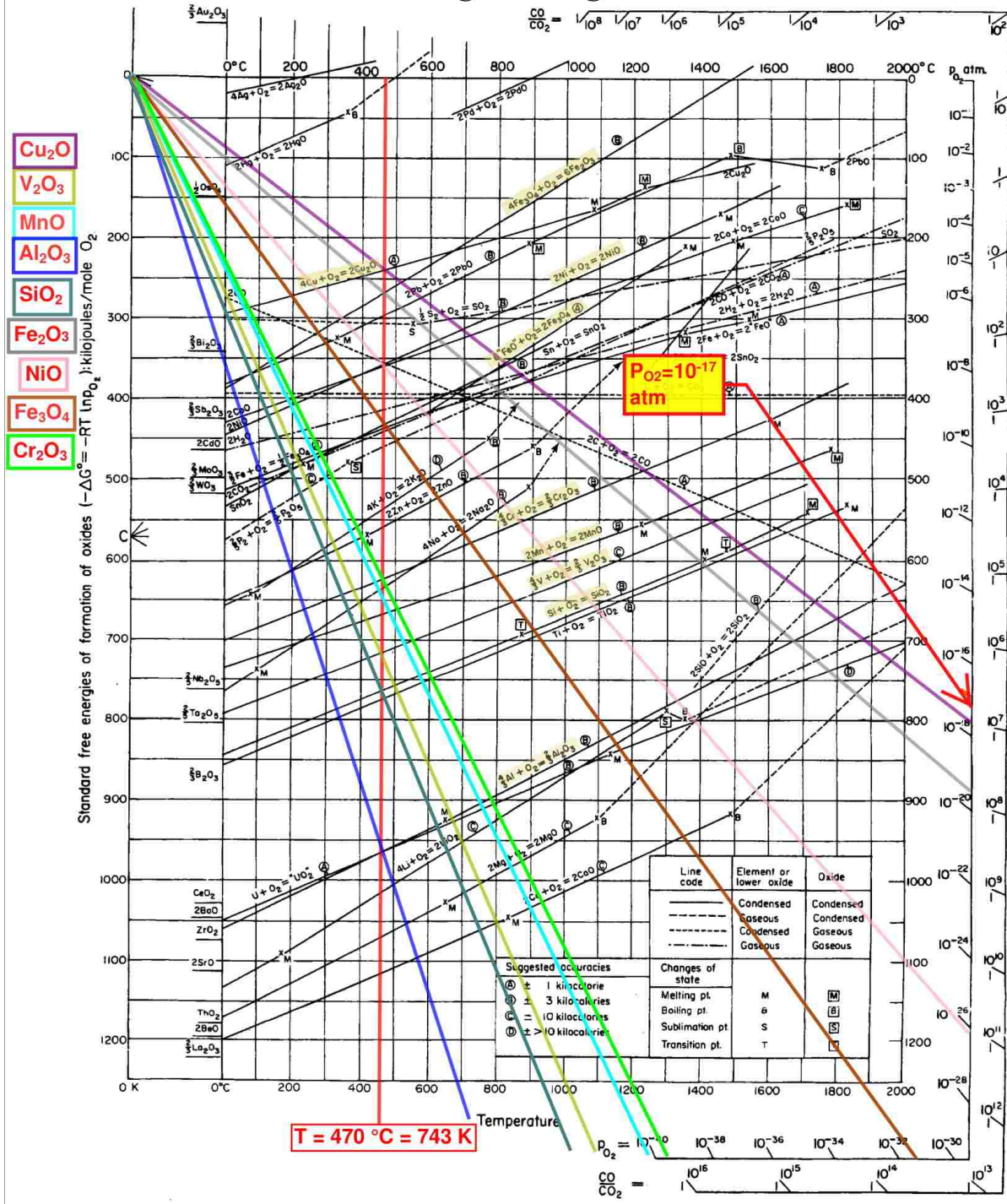
Figure 10: Ellingham Diagram

Since the Ellingham diagram does not contain the formation lines for uncommon metals such as tungsten, molybdenum, cerium, and niobium, binary phase diagrams were used to determine stable oxides for these alloying elements. Two such diagrams for the binary systems of tungsten-oxygen and niobium-oxygen are shown in Figures 11 and 12, respectively [25]. The experimental LBE oxygen concentration and temperature are used to predict the formation of tungsten (IV) oxide, WO_2. The phase diagram for the niobium-oxygen system showed that niobium (II) oxide, NbO, is stable under the given experimental conditions. Phase diagrams for the systems of cerium-oxygen and molybdenum-oxygen are not conclusive regarding thermo-dynamically stable oxides. Thus, the oxidation reactions of alloying elements cerium and molybdenum are omitted from the simulation. An updated list of elements and corresponding oxidation reactions character-ized in the present model is compiled in Table 9.
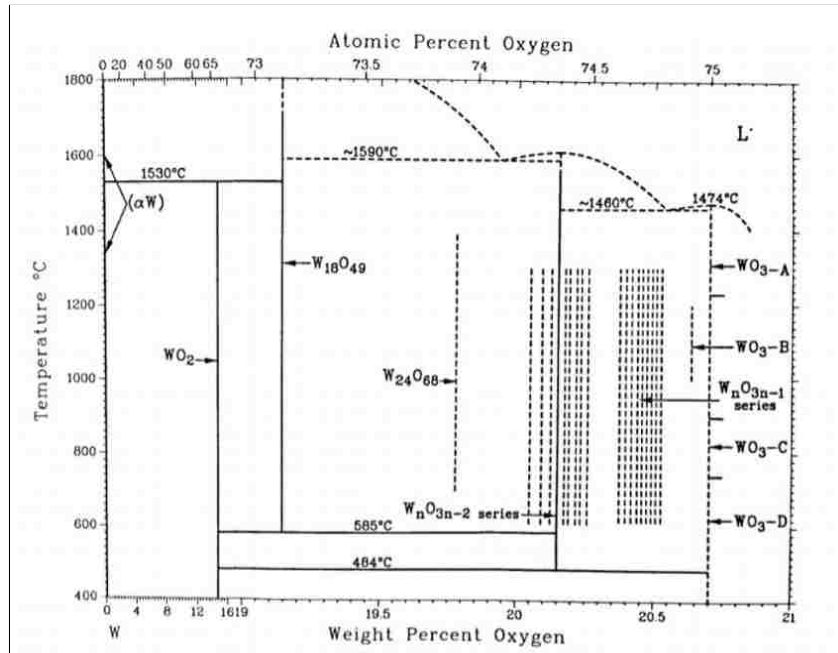
Figure 11: Phase Diagram of W-O system [25]
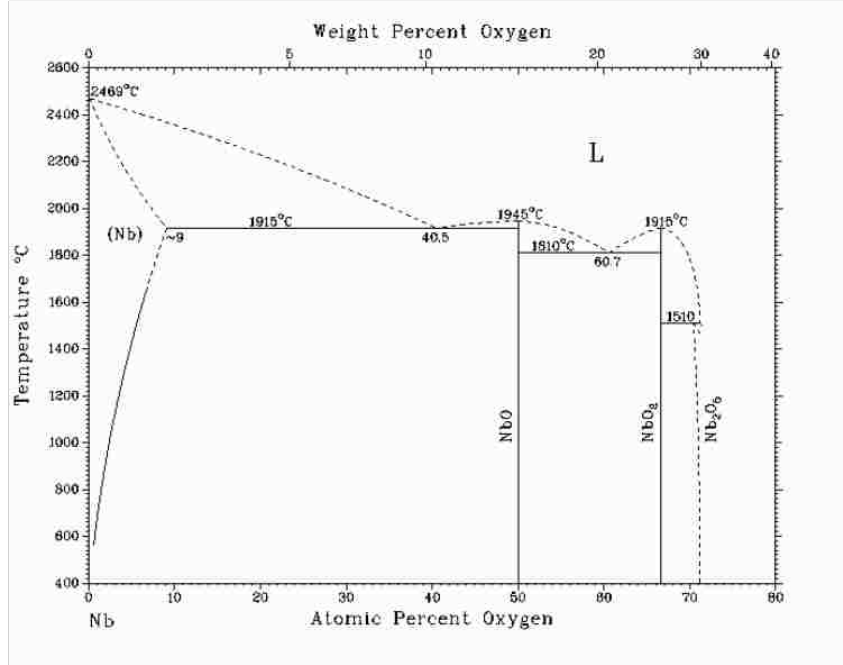
Figure 12: Phase Diagram of Nb-O system [25]

Table 9: Elements and Related Oxidation Reactions Simulated in Oxidation Model

Alloying Element	Symbol	Oxidation Reaction	IUPAC Name of Oxide
Copper	Cu	$2\mathrm{Cu} + \frac{1}{2}\mathrm{O}_2 \longrightarrow \mathrm{Cu}_2\mathrm{O}$	Copper(I)Oxide
Aluminum	Al	$\frac{2}{3}\mathrm{Al} + \frac{1}{2}\mathrm{O}_2 \longrightarrow \frac{1}{3}\mathrm{Al}_2\mathrm{O}_3$	Aluminium(III)Oxide
Niobium	Nb	$\mathrm{Nb} + \frac{1}{2}\mathrm{O}_2 \longrightarrow \mathrm{NbO}$	Niobium(II)Oxide
Vanadium	V	$\frac{2}{3}\mathrm{V} + \frac{1}{2}\mathrm{O}_2 \longrightarrow \frac{1}{3}\mathrm{V}_2\mathrm{O}_3$	Vanadium(III)Oxide
Manganese	Mn	$\mathrm{Mn} + \frac{1}{2}\mathrm{O}_2 \longrightarrow \mathrm{MnO}$	Manganese(II)Oxide
Tungsten	W	$\frac{1}{2}\mathrm{W} + \frac{1}{2}\mathrm{O}_2 \longrightarrow \frac{1}{2}\mathrm{WO}_2$	Tungsten(IV)Oxide
Nickel	Ni	$\mathrm{Ni} + \frac{1}{2}\mathrm{O}_2 \longrightarrow \mathrm{NiO}$	Nickel(II)Oxide
Silicon	Si	$\frac{1}{2}\mathrm{Si} + \frac{1}{2}\mathrm{O}_2 \longrightarrow \frac{1}{2}\mathrm{SiO}_2$	Silicon(IV)Oxide
Chromium	Cr	$\frac{2}{3}\mathrm{Cr} + \frac{1}{2}\mathrm{O}_2 \longrightarrow \frac{1}{3}\mathrm{Cr}_2\mathrm{O}_3$	Chromium(III)Oxide
Iron	Fe	$\frac{3}{4}\mathrm{Fe} + \frac{1}{2}\mathrm{O}_2 \longrightarrow \frac{1}{4}\mathrm{Fe}_3\mathrm{O}_4$	Iron(II,III)Oxide
		$2\mathrm{Fe}_3\mathrm{O}_4 + \frac{1}{2}\mathrm{O}_2 \longrightarrow 3\mathrm{Fe}_2\mathrm{O}_3$	Iron(III)Oxide

Now the parameter, mass fraction r of element M in its respective oxide, $M_x O_y$, is calculated using

$$r = \frac{\text{x} \cdot \text{Atomic Mass } M}{\text{x} \cdot \text{Atomic Mass } M + \text{y} \cdot \text{Atomic Mass O}}. \tag{67}$$

4.2.3 Oxygen Concentrations at Surface, Inner Oxide/Interface Boundary and Interior

From the assumptions made in Chapter 2, the surface concentration of oxygen is set to a constant saturated supply of 100 at.-%O.

To evaluate C_{MO}, the solubility of oxygen in the alloy is discussed. The class of steels to which EP-823 belongs are subject to extensive deoxidization in the steelmaking cooling process. Therefore the oxygen concentration solubility limit of the steel is estimated by utilizing both the weight ratio of carbon in Table 7 and equation (68), which relates atomic oxygen content and carbon content in pre-cooled liquid steel [26].

$$\text{wt.-\%Carbon in alloy} \times \text{wt.-\%Oxygen in alloy} = 0.0025 \tag{68}$$

By converting the weight ratio of carbon in Table 7 to a weight percent of 0.17 wt.-%C, a weight percent of oxygen in pre-cooled steel of 0.015 wt.-%O is obtained. The conversion of the weight percent oxygen to atomic percent oxygen involves the following. First the weight ratio of each alloying element, w, is converted to mass of the element per 100 g alloy, w_i. The calculated weight percent of oxygen from equation (68) is also converted to mass of oxygen per 100 g alloy. This value is also included in the list of w_i. Next, w_i is divided by the atomic mass of each alloying element, M_i, to obtain moles of each element M per 100 g alloy, denoted X_i. The values of X_i are summed to obtain total moles of alloy per 100 g alloy, denoted X. Each value of X_i is divided by X to obtain the atomic ratio of atoms of the respective alloying element to total atoms of alloy, a_i. The task of finding atomic percent of each element, listed in the right column of Table 10, is achieved.

Thus, the atomic percent of the oxygen concentration solubility is estimated to be 0.05 at.-%O and, as mentioned in Chapter 2, is set as the value for the interface parameter C_{MO} in the present model. It should be noted that this value is generous because it exceeds the actual oxygen solubility limit for EP-823, as steels belonging to this class lose much of the pre-cooled oxygen content during solidification.

Two assumptions are made regarding the composition of the oxide layer for the purpose of evaluating C_{OM}. As mentioned in Chapter 2, the oxide layer is comprised of both a compact inner sublayer and a porous outer sublayer. The first assumption is that the inner sublayer is purely comprised of iron (II,III) oxide, Fe_3O_4. This assumption is based on experimental studies indicating that Fe_3O_4, commonly known as magnetite, is the primary component of the oxide layer [27]. This assumption reserves the porous outer

Table 10: Weight Percent to Atomic Percent for Alloying Elements of EP-823

	Atomic Mass of M g/mol	g M/100g alloy	mol M/100g alloy	Atomic Percent M
	M_i	w_i	X_i	$100*a_i$
Element				
Boron	10.811	0.005	0.0005	0.03
Carbon	12.0107	0.17	0.0142	0.77
Oxygen	15.9994	0.015	0.0009	0.05
Aluminium	26.9815386	0.02	0.0007	0.04
Silicon	28.0855	1.11	0.0395	2.16
Phosphorus	30.973762	0.005	0.0002	0.01
Sulfur	32.065	0.004	0.0001	0.01
Vanadium	50.9415	0.34	0.0067	0.37
Chromium	51.9961	11.69	0.2248	12.31
Manganese	54.938045	0.54	0.0098	0.54
Iron	55.845	84	1.5042	82.34
Nickel	58.6934	0.65	0.0111	0.61
Copper	63.546	0.01	0.0002	0.01
Niobium	92.90638	0.26	0.0028	0.15
Molybdenum	95.96	0.7	0.0073	0.40
Cerium	140.116	0.08	0.0006	0.03
Tungsten	183.84	0.6	0.0033	0.18

sublayer for the oxides listed in Table 9. One case in which both layers are comprised of magnetite is also simulated. Thus, the value for C_{OM} is fixed to the atomic percent of oxygen in Fe_3O_4 which is calculated by

$$C_{OM} = \frac{4\,\text{atoms O}}{3\,\text{atoms Fe} + 4\,\text{atoms O}} = \frac{4}{7} = 57\,\text{at.-\%O}. \tag{69}$$

Lastly, the atomic percent of oxygen at the unexposed front, $C_{M\infty}$ is assumed to be $0\,\text{at.-\%O}$.

While in Chapter 2 the oxygen concentration is defined as molar density with dimensions $[\text{molL}^-3]$, the atomic percent of oxygen is akin to the non-dimensional molar density. The atomic percent of oxygen at each boundary of the planar model is shown in Figure 13. The profile of the predicted oxygen concentration pattern is also drawn.
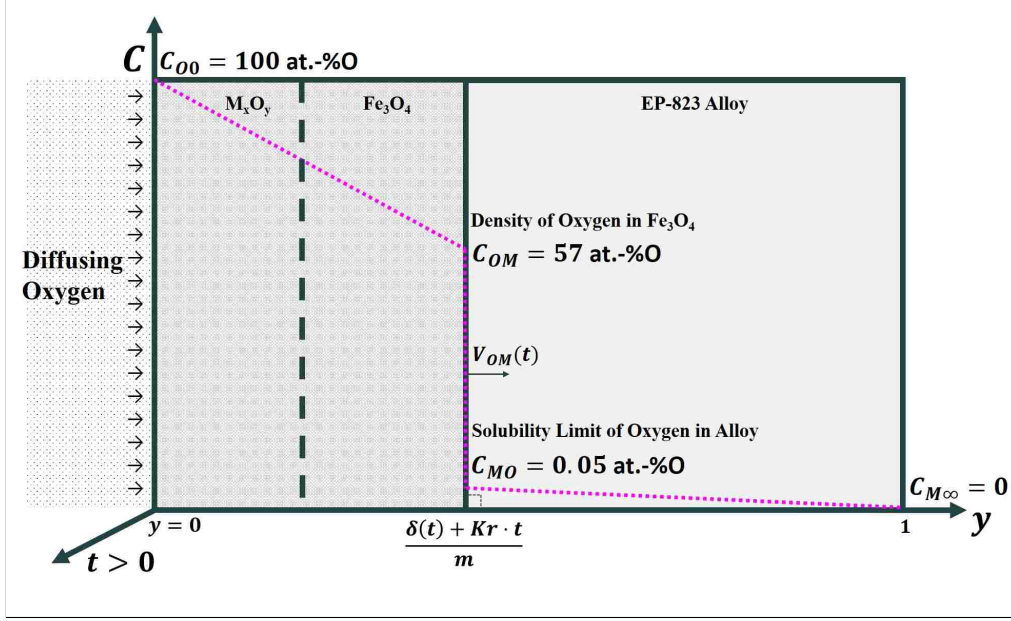
Figure 13: Input Parameter Values for Boundary Oxygen Concentration

4.2.4 Densities of Metal Phase and Inner and Outer Oxide Layers

The density of the alloy, ρ_{Me}, is specified to be $7.87\,\mathrm{g/cm^3}$, which is the approximate density of a class of low alloy carbon steels to which EP-823 belongs [28]. It follows from the assumption of composition of the inner oxide layer that its density, ρ_{in}, is fixed to that of Fe_3O_4. The density of the outer layer, ρ_{out}, is in accordance with the oxide from Table 9 being considered.

4.2.5 Contribution of Reactive M to Inner Oxide Layer Formation

The value of the ratio of reactive atoms of element M contributing to the inner oxide layer to the total reactive M atoms, p, is set to 0.8. This assumption is also based on the work of Wagner, who had found an uneven distribution of cations in the oxide layer [12].

4.2.6 Scale Removal Rate

The manner in which the parameter K_r, scale removal rate is obtained is described. Scale removal is described as the tendency of the flowing liquid to remove the oxide layer surface by means of ablation and erosion. It is commonly known as the corrosion rate or the recession rate. In the analysis of the experiments, Zhang approximated the scale removal rate in the mentioned experimental conditions by a solution based on both Tedmon's oxidation-evaporation model [1]. The Tedmon relation, when applied to the oxidation-ablation model is given by equation (70) [14]. The linear scale removal term, K_r, is subtracted from the parabolic oxide layer growth term, $\frac{k_p}{\delta(t)}$, wherein k_p is the parabolic growth constant derived in Appendix

B. As the thickness of the oxide layer increases, the rate of oxidation decreases due to the fact that oxygen atoms must travel farther. This is modeled by parabolic growth.

$$\frac{d\delta(t)}{dt} = \frac{k_p}{\delta(t)} - K_r \tag{70}$$

Although the calculation of k_p is not directly explained in the report by Zhang, it is assumed the parabolic rate law (Appendix B) was fitted to experimental times, t_{exp}, and corresponding experimental oxide layer thicknesses, δ_{exp} whereby k_p is determined. If the steady state is applied to equation (70), then the steady state or asymptotic thickness, δ_s, can be expressed by

$$K_r = \frac{k_p}{\delta_s}. \tag{71}$$

By substitution of equation (71) into equation (70), the first order non-linear ODE given by equation (72) is obtained.

$$\frac{d\delta(t)}{dt} = \frac{k_p}{\delta(t)} - \frac{k_p}{\delta_s} \tag{72}$$

Because no general solution exists for this type of equation, a solution for oxide layer thickness, shown in equation (73), is approximated by Zhang [1].

$$\delta(t) = (2k_p t)^{\frac{1}{2}} - \frac{2}{3}\frac{k_p}{\delta_s}t \tag{73}$$

By equation (73), δ_s is obtained by substitution of corresponding t_{exp} and δ_{exp}. Finally, K_r is obtained by substituting the fitted k_p value and δ_s into equation (71).

From the data obtained by Zhang, the value of K_r for the given experimental conditions is given as $1.572 \times 10^{-13}\,\mathrm{m\,s^{-1}}$ [1]. The corresponding k_p value was determined to be $1.124 \times 10^{-17}\,\mathrm{m^2/s}$.

4.2.7 Diffusion Coefficient of Oxygen

The diffusion coefficient of oxygen within the oxidation plane is dependent on the partial pressure of oxygen in the surrounding fluid, the type of surrounding fluid, the composition of the oxide and metal phases, the partial pressure of hydrogen, and the total pressure of the fluid which is exerted on the material.

Experimental data on diffusion coefficients of oxygen in oxides which considers the present simulation environment is lacking. However, experiments had been conducted on magnetite, Fe_3O_4, at higher partial pressures of oxygen in water, which is the surrounding medium [29]. The reported diffusion coefficients at a temperature of $500\,\degree C$ are on the order of $1 \times 10^{-10}\,\mathrm{\mu m^2/s}$. This is the value used for D_{Ox} for the entire

oxide layer in the present simulation.

Experimental data on oxygen diffusion in EP-823 alloy and the class of martensitic steels to which it belongs is also limited. For D_{Me} the value of D_{Ox} was divided by 4. This is based on the assumption that the diffusion of oxygen oxide layer is facilitated by the porosity of the layer. Thus, D_{Me} is given a value of $2.5 \times 10^{-11}\,\mathrm{\mu m^2/s}$ in the present simulation.

While the non-dimensional value, $\bar{D}_{Me}$ is set to 1, as mentioned in Chapter 2, the nondimensional value, $\bar{D}_{Ox}$, varies based on density, ρ_{out}, weight ratio w, and mass fraction r, because all are factored into the value of m, which is defined in equation (18). Equation (49) demonstrates how m and $\bar{D}_{Ox}$ are related.

The list of input parameters used for the numerical simulation is compiled in Table 11.

Table 11: Input Parameters

Element M	w	Atomic Mass g/mol	Oxide	rho$_{out}$ g/cm^3	Molar Mass g/mol	r	rho$_{in}$ g/cm^3	rho$_{Me}$ g/cm^3	K$_r$ m/s	D$_{Ox}$ m$^2/s$	D$_{Me}$ m$^2/s$	p	m
Cu	0.0001	63.546000	Cu$_2$O	6.000	143.0900	0.888196	5.15	7.86	1.572E-13	1.00E-22	2.50E-23	0.8	0.000166964
Al	0.0002	26.981539	Al$_2$O$_3$	3.987	101.9600	0.529257	5.15	7.86	1.572E-13	1.00E-22	2.50E-23	0.8	0.000610384
Nb	0.0026	92.906380	NbO	7.300	108.9060	0.853088	5.15	7.86	1.572E-13	1.00E-22	2.50E-23	0.8	0.004377527
V	0.0034	50.941500	V$_2$O$_3$	4.870	149.8810	0.679759	5.15	7.86	1.572E-13	1.00E-22	2.50E-23	0.8	0.007721551
Mn	0.0054	54.938050	MnO	5.430	70.9374	0.774458	5.15	7.86	1.572E-13	1.00E-22	2.50E-23	0.8	0.010531954
W	0.0060	183.850000	WO$_2$	10.800	215.8390	0.851792	5.15	7.86	1.572E-13	1.00E-22	2.50E-23	0.8	0.009625772
Ni	0.0065	58.693400	NiO	6.670	74.6928	0.785797	5.15	7.86	1.572E-13	1.00E-22	2.50E-23	0.8	0.012049220
Si	0.0111	28.085000	SiO$_2$	2.196	60.0800	0.467460	5.15	7.86	1.572E-13	1.00E-22	2.50E-23	0.8	0.045990407
Cr	0.1169	51.996100	Cr$_2$O$_3$	5.220	151.9904	0.684202	5.15	7.86	1.572E-13	1.00E-22	2.50E-23	0.8	0.260063187
Fe	0.8400	55.847000	Fe$_3$O$_4$	5.150	231.5330	0.723616	5.15	7.86	1.572E-13	1.00E-22	2.50E-23	0.8	1.771684554
Fe	0.8400	55.847000	Fe$_2$O$_3$	5.240	159.6900	0.699443	5.15	7.86	1.572E-13	1.00E-22	2.50E-23	0.8	1.826619376

The present model, which had been previously developed to model the oxidation of pure titanium, was modified for the current simulation. It uses 500 nodes with a time step of 0.01s [6]. Per time step, the number of iterations is 2. Thus the accuracy is set as $\epsilon = 10^{-4}$ [6]. The simulation produces results which are non-dimensional with respect to oxygen concentration and dimensional with respect to space and time. The original length of the metal plane is set to $70\,\mathrm{\mu m}$. The simulation was run for physical times of 0.5 h, 1 h, 2 h, 4 h, 8 h, 16 h, 32 h, 64 h, 128 h, and 250 h for each oxide.

Chapter 5 Results and Discussion

5.1 Concentration Profile

The progression of oxide layer growth for the successive time interval simulations is shown. The oxygen concentration, C, is plotted as a function of the distance from the exposed surface, which is the continually renewed calculating coordinate mentioned in Chapter 2. Figure 14 shows these plots. The extent to which the oxide/metal interface moves inward with respect to the original thickness of the specimen, 70 μm, can be seen. The profile of the concentration matches the prediction in Figure 13 in Chapter 4.
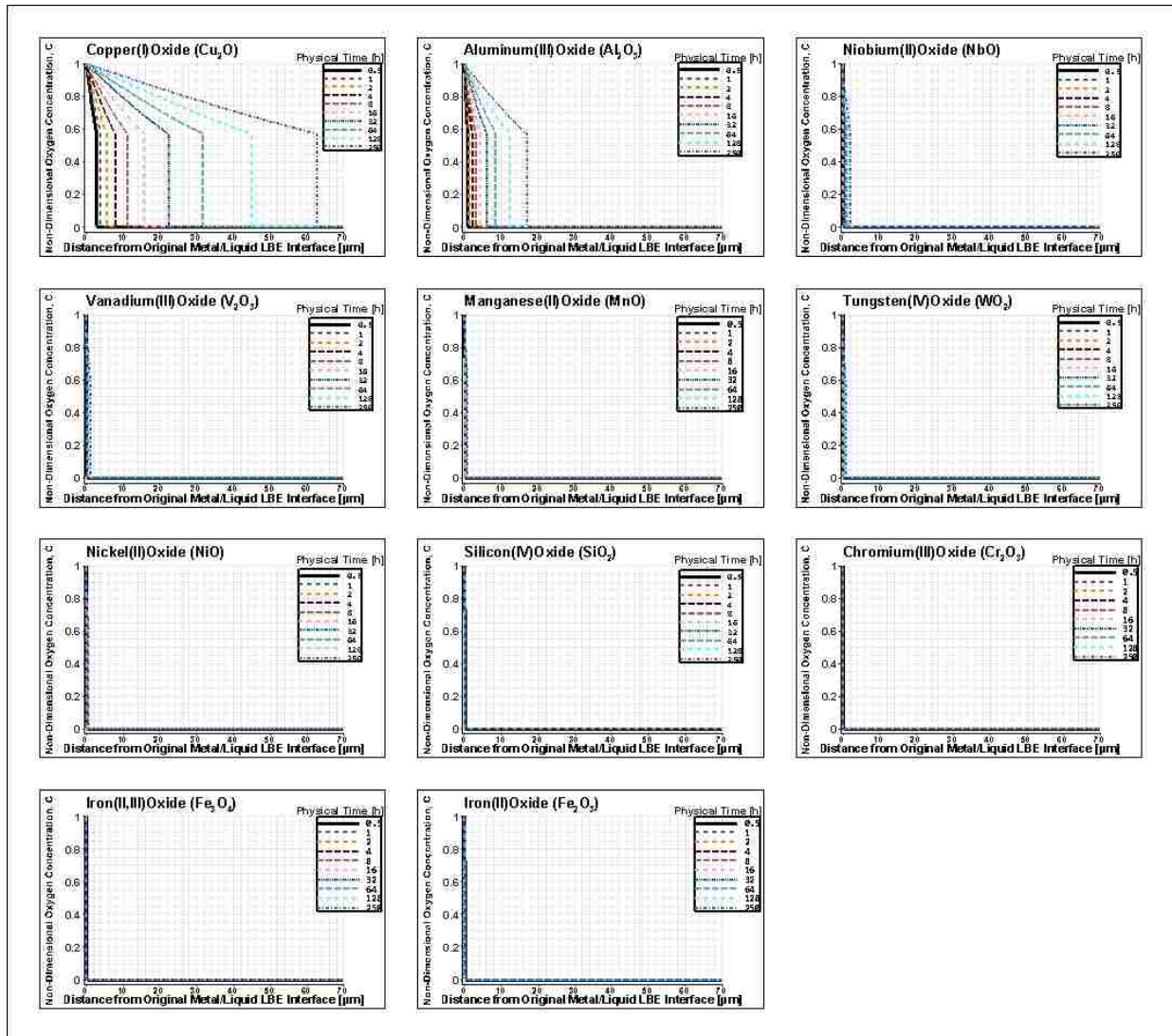

Figure 14: Non-Dimensional Oxygen Concentration Profile v. Distance

In general, the concentration decrease from the surface inward is linear until it reaches the interface where a negative jump in concentration is seen. Per simulation, the boundary and oxide metal interface

concentrations remain at the atomic percent values mentioned in Chapter 4. It is evident in Figure 14 that Al_2O_3 and Cu_2O exhibit the greatest inward growth, whereas the remaining oxides show inward growth which is less than $5\,\mu m$ at the greatest time interval of $250\,h$.

The thicknesses for each oxide at each time interval are shown in Table 12. It is evident from this table as well, that the growth of the oxide layer for Al_2O_3 and Cu_2O is the greatest. For the remaining oxides, it can be seen that the growth is limited. For the iron and chromium oxides, no change in thickness is seen at all. Evaluation of the stability criterion for the number of nodes used for the simulation of oxide growth for these oxides would be of help. The optimal value of the convergence accuracy, ϵ, chosen for the simulation must be assessed and must be adjusted accordingly such that the oxide layer thicknesses derived from the model are more accurate. In the present model, the convergence accuracy, ϵ, and number of nodes, N are assigned uniform values for all oxide simulations. The assessment of stability and convergence for the simulation of oxide growth for each oxide must include the all the values in the dimensionless factor m, which have direct bearing on the oxide layer oxygen diffusivity, D_{Ox} in the model. Because all stainless steels, including EP-823 alloy, are comprised primarily of iron, the lack of oxide layer growth due to iron composition does not make sense.

One explanation for this may be the fact that the model, at a maximum interval of $250\,h$ can only apply to incipient oxidation. It can be argued that running the simulations for greater time intervals may lead to the evolution of an oxide layer with a finite thickness.

Table 12: Oxide Layer Thickness Values from Simulation

Time (h)	Cu₂O	Al₂O₃	NbO	V₂O₃	MnO	NiO	WO₂	SiO₂	Cr₂O₃	Fe₂O₃	Fe₃O₄	
0.5	2.80561096	0.84168336	0.14028056	0.14028056	0.14028056	0.14028056	0.14028056	0.14028056	0.14028056	0.14028056	0.14028056	Oxide
1	3.92785592	1.12224492	0.14028052	0.14028052	0.14028052	0.14028052	0.14028052	0.14028052	0.14028052	0.14028052	0.14028052	Layer
2	5.61122284	1.54308584	0.28056114	0.14028054	0.14028054	0.14028054	0.14028054	0.14028054	0.14028054	0.14028054	0.14028054	Thickness
4	7.99599168	2.24448868	0.28056108	0.14028058	0.14028058	0.14028058	0.14028058	0.14028058	0.140280568	0.14028058	0.14028058	(micron)
8	11.22244736	3.08617236	0.42084166	0.28056116	0.14028056	0.14028056	0.28056116	0.14028056	0.14028056	0.14028056	0.14028056	
16	15.85170472	4.34869772	0.70140282	0.42084172	0.28056112	0.28056112	0.28056112	0.14028052	0.14028052	0.14028052	0.14028052	
32	22.44488944	6.17234444	0.84168334	0.42084164	0.42084164	0.28056114	0.42084164	0.14028054	0.14028054	0.14028054	0.14028054	
64	31.84368888	8.69739488	1.26252488	0.70140278	0.56112228	0.42084168	0.56112228	0.14028058	0.14028058	0.14028058	0.14028058	
128	45.03005776	12.34468776	1.68336676	0.98196396	0.70140276	0.70140276	0.84168336	0.14028056	0.14028056	0.14028056	0.14028056	
250	62.84569	17.25451	2.38477	1.402806	0.9819639	0.8416834	1.1222445	0.2805611	0.15831663	0.140280561	0.140280561	

The concentration profile of NbO, which is among the oxides displaying minimal growth, is magnified in Figure 15.
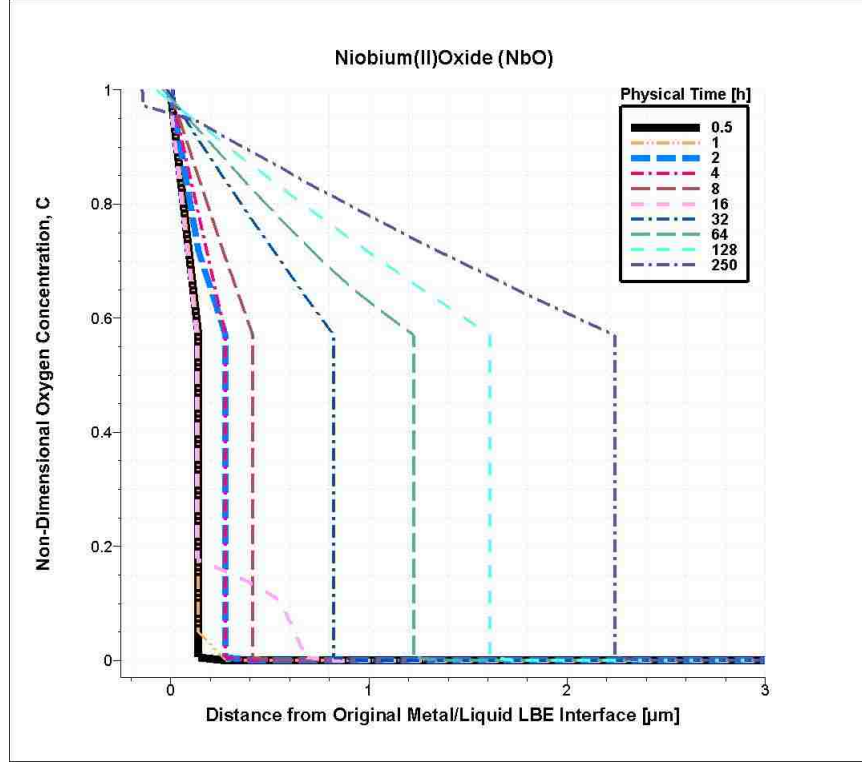
Figure 15: Concentration Profile of Niobium II Oxide

5.2 Steady State Thickness

The semi-empirical method Zhang [1] uses to approximate the steady state thickness, δ_s, which is described in Chapter 4, is applied to the present simulation. For each reaction listed in Table 9, the results of the simulations are evaluated in the following manner:

1. The parabolic rate constant, k_p, is determined.

2. The steady state thickness, δ_s, is determined by the Tedmon equation (70).

3. The steady state thickness, δ_s, is approximated by equation (73).

5.2.1 Power Law

As mentioned in Chapter 4, the simulation for each reaction is run for a series of physical time intervals, the maximum time period of which is $250\,\mathrm{h}$. As mentioned, with respect to the progression of oxidation on stainless steel, these reaction times are considered incipient; thus, this analysis is limited to oxidation kinetics during initial exposure of the metal alloy to the oxidizing environment.

For each time interval, corresponding data indicating oxide layer thickness, δ, is obtained from the simulation. In order to determine the extent to which parabolic growth is obeyed, oxide layer thickness data

values are plotted versus the corresponding time interval values as shown in Figure 16. The data values are organized in Table 12.

A power law regression is applied to the distribution of the plot of each reaction.
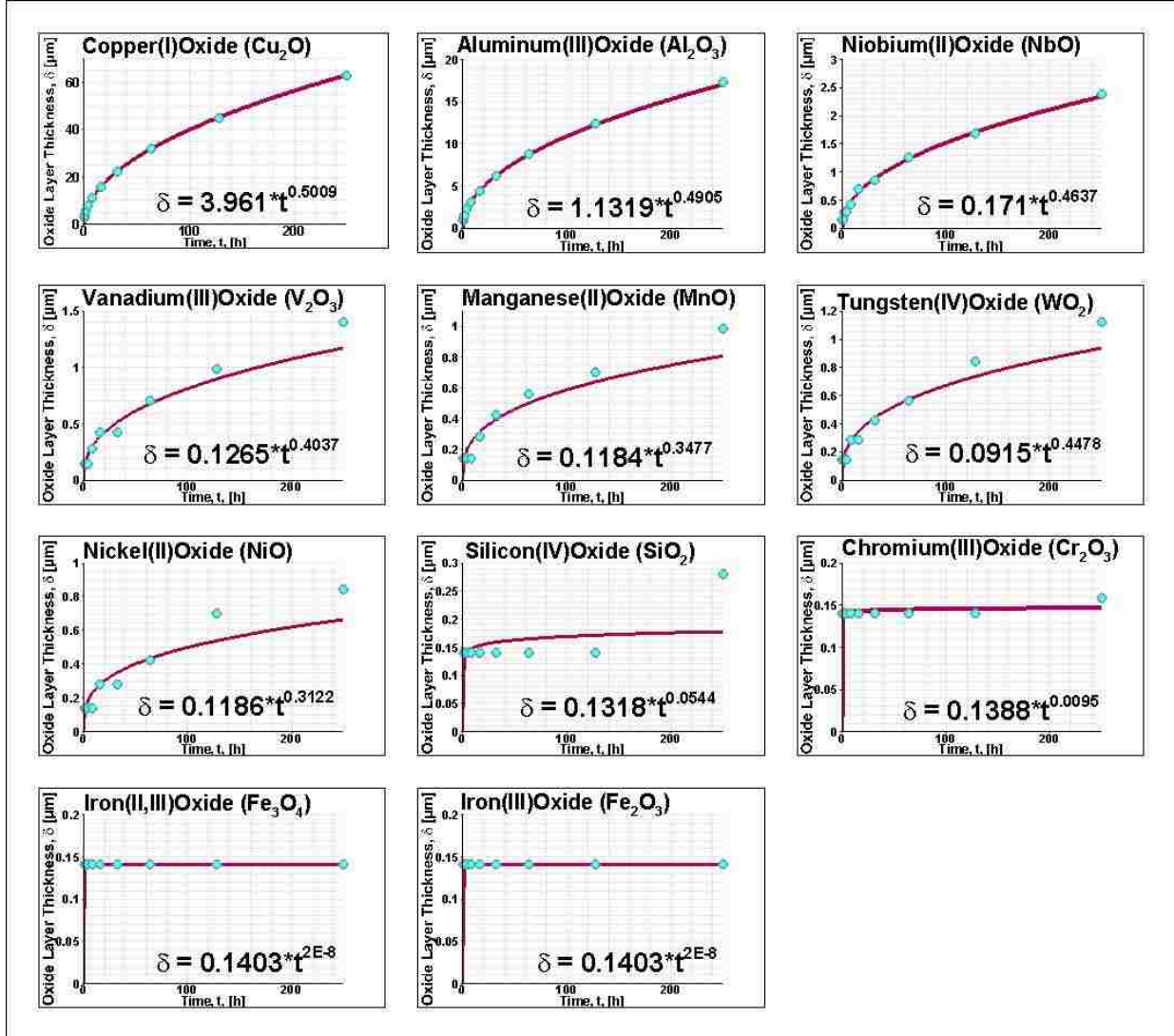
Figure 16: Oxide Layer Thickness Data v. Time Fit to Power Law

Based on the model proposed by Wagner [12], an ideal regression equation for parabolic growth would be of the form

$$\delta = (2k_p t)^{0.5}. \tag{74}$$

It can be seen in Figure 16 that while certain growth rates are reasonably close to the parabolic case, as in the oxide formations of Cu_2O, Al_2O_3, NbO, and WO_2, the remaining oxides show growth patterns which deviate, in varying degrees, from Wagner's model. The foregoing discussion on modifying stability and convergence criteria for each oxide applies here as well.

5.2.2 Parabolic Rate Constant

To predict δ_s using the steady state Tedmon equation (71) or the approximation made by Zhang [1] in equation (73), k_p is needed. To this end, the squares of the oxide layer thickness values in Table 12 are plotted against the respect time intervals as shown in Figure 17; a linear regression is applied assuming that the initial oxide layer thickness is zero.
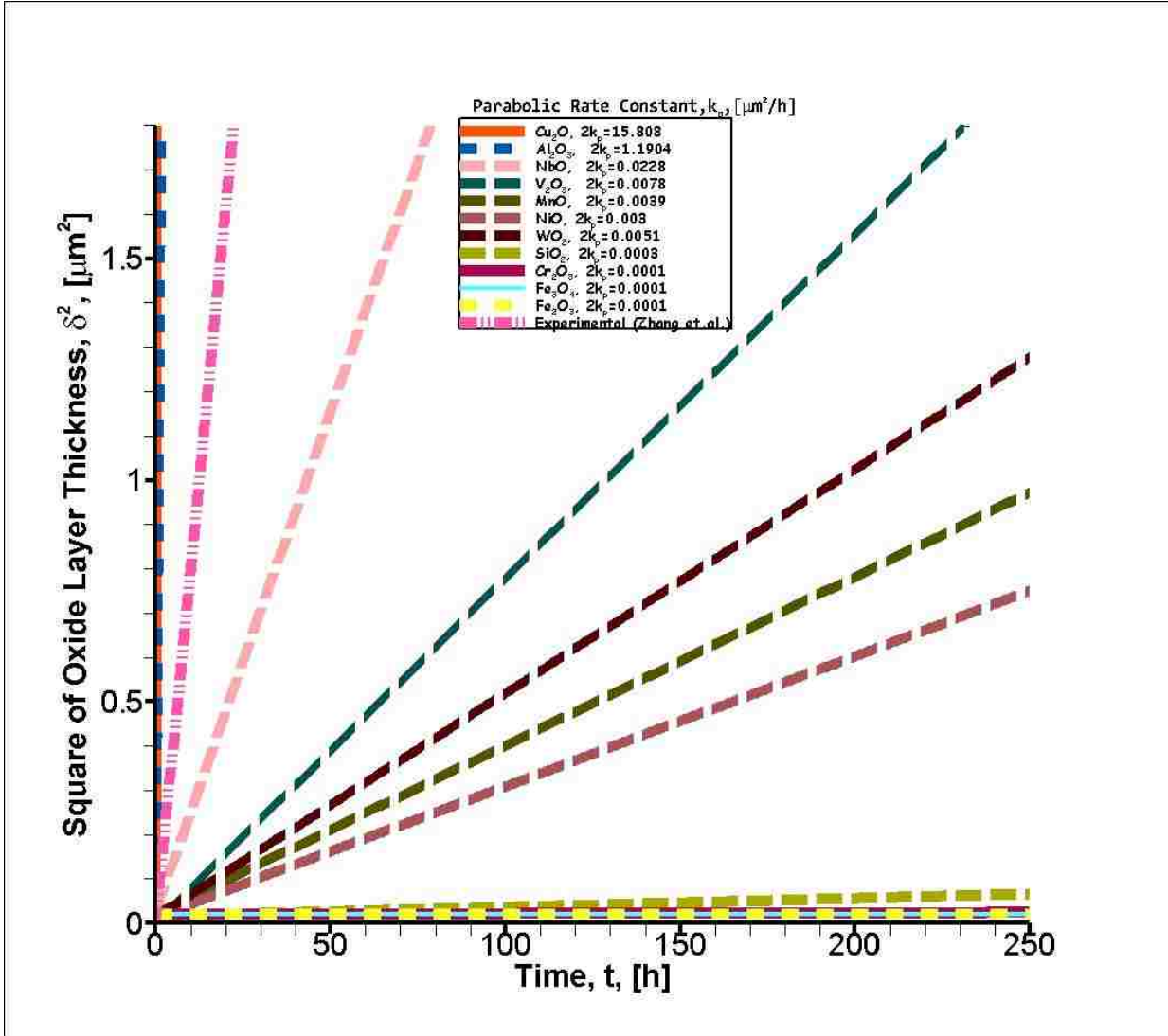
Figure 17: Squares of Oxide Layer Thickness Data v. Time

For each reaction, the slope of the regression, gives a value twice the parabolic rate constant, $2 \cdot k_p$, according to equation (74). The values determined for k_p are shown in Table 13. These values as well as the values for the interval times, t, are substituted into equation (74) to obtain parabolic curves depicted in Figure 18.

Table 13: Parabolic Rate Constant Values, k_p

	Cu_2O	Al_2O_3	NbO	V_2O_3	MnO	NiO	WO_2	SiO_2	Cr_2O_3	Fe_2O_3	Fe_3O_4
$2k_p(micron^2/h)$	1.58E+01	1.19E+00	2.28E-02	7.80E-03	3.90E-03	3.00E-03	5.10E-03	3.00E-04	1.00E-04	1.00E-04	1.00E-04
$k_p(micron^2/h)$	7.90E+00	5.95E-01	1.14E-02	3.90E-03	1.95E-03	1.50E-03	2.55E-03	1.50E-04	5.00E-05	5.00E-05	5.00E-05
$k_p(micron^2/s)$	2.20E-03	1.65E-04	3.17E-06	1.08E-06	5.42E-07	4.17E-07	7.08E-07	4.17E-08	1.39E-08	1.39E-08	1.39E-08
$k_p(m^2/s)$	2.20E-15	1.65E-16	3.17E-18	1.08E-18	5.42E-19	4.17E-19	7.08E-19	4.17E-20	1.39E-20	1.39E-20	1.39E-20
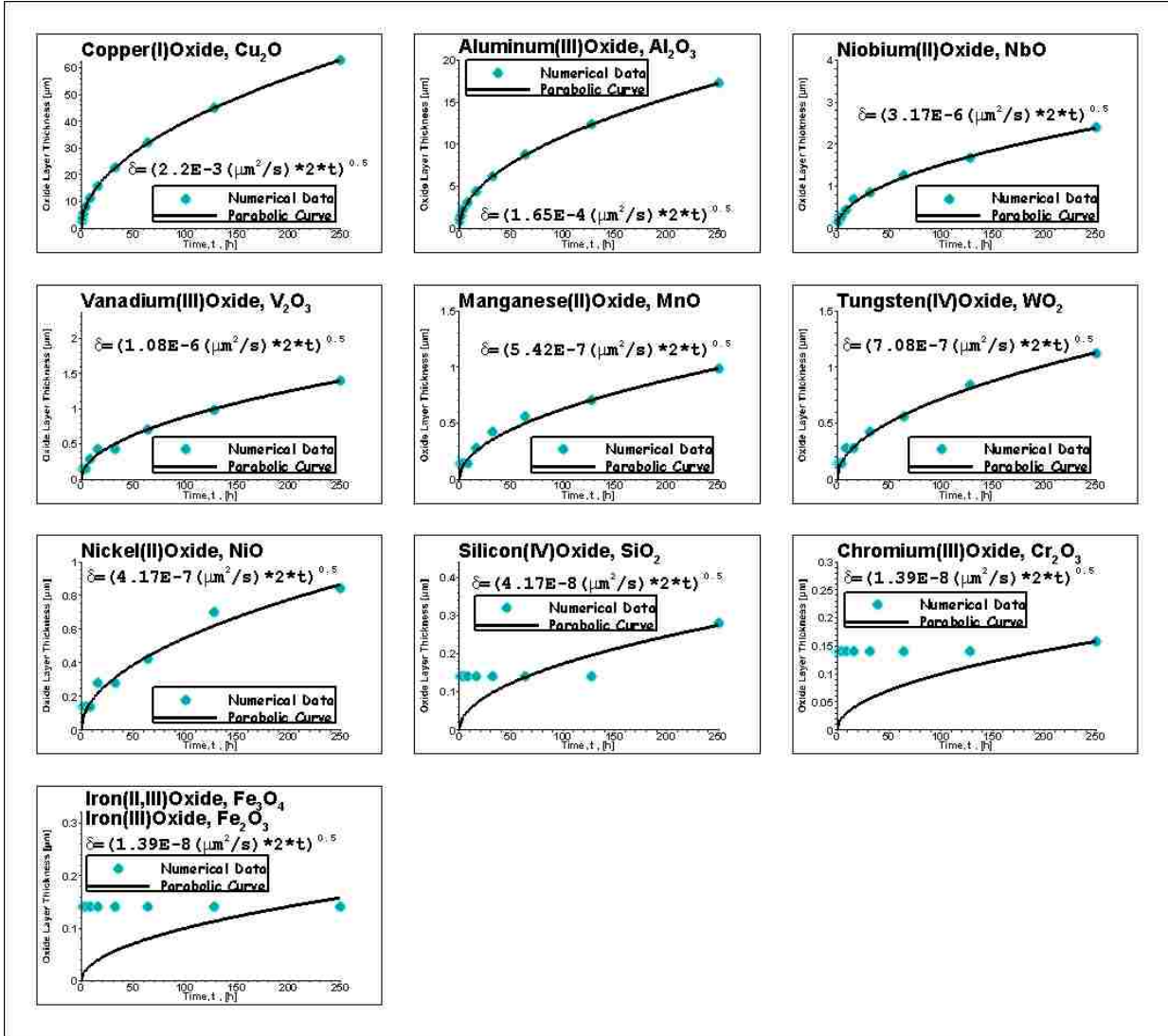
Figure 18: Oxide Layer Thickness Data v.Time Fit to Parabolic Law

The experimental value of k_p for EP-823 alloy reported by Zhang at $3000\,\text{h}$ exposure [1], determined to be $1.124 \times 10^{-17}\,\text{m}^2/\text{s}$, falls between the k_p values calculated for Al_2O_3 and NbO as shown in Figure 17. A direct explanation for this cannot be deduced without the optimization of stability and convergence criteria.

For future work, the consideration of the tendency of selective oxidation of certain alloying metals to effect a parabolic growth rate is ideal. This tendency is better explained by referencing the Ellingham diagram shown in Figure 10. The lower the oxidation reaction curve of a certain element with respect to the free energy of formation axis, the more likely the oxidation of this element. Furthermore, at a given temperature and alloying element composition, the oxidation of the element corresponding to the bottom most reaction line is favored [22]. In other words, the reaction with the lowest free energy of formation requirement competes with other concurrent isothermal reactions by reducing the oxides with a higher free

44

energy. In the case of the alloying metals considered for the present simulation, the oxidation of aluminum and silicon are suppositive over the oxidation of each of the remaining alloys. Thus, the role of the copper oxide layer growth rate is the effective parabolic growth rate for EP-823 is perhaps limited by other more likely reactions. While a conclusive method to reconcile parabolic rate constants for the oxides of each individual oxide with the overall rate constant for the alloy does not exist, examining selective oxidation of certain alloying elements clarifies some ambiguity.

Further discussion involves the tendency of more than one alloying element to form a single oxide. This phenomena, referred to as co-precipitation of oxides, has been reported in corrosion experiments [1, 30]. For example, evidence of the formation of iron-chromium spinel oxides of the form $(Fe_xCr_{1-x})_3O_4$ has been often seen in the oxide layer after 1000 h exposure to LBE in conditions similar to the experiments conducted by Zhang [1, 30, 31]. In fact, it is unlikely that the oxide layer contains portions of pure single metal oxides. Rather, these co-precipitates, or spinel oxides are the common by-product. In order for spinel formation, the thermodynamics and kinetics of the reaction as well as maintenance of matched or unmatched oxidation states of the co-precipitating elements, and stability of the crystal structure of the oxide are factors. The oxidation states of the metals in the corresponding oxides are listed in Table 14.

Table 14: Oxidation States of Metals in Metal Oxides, Ionic Radii, and Crystal Structures

Alloying Element	Symbol	Oxide	IUPAC Name of Oxide	Metal Oxidation State	Ionic Radius [nm]	Crystal Structure	Calculated k_p [m^2/s]
Copper	Cu	Cu_2O	Copper(I)Oxide	+1	0.077	FCC	2.20E-15
Aluminum	Al	Al_2O_3	Aluminium(III)Oxide	+3	0.053	FCC, HCP	1.65E-16
Niobium	Nb	NbO	Niobium(II)Oxide	+2			3.17E-18
Vanadium	V	V_2O_3	Vanadium(III)Oxide	+3	0.088	HCP	1.08E-18
Manganese	Mn	MnO	Manganese(II)Oxide	+2	0.067	SC	5.42E-19
Tungsten	W	WO_2	Tungsten(IV)Oxide	+4		Cubic	7.08E-19
Nickel	Ni	NiO	Nickel(II)Oxide	+2	0.069	FCC	4.17E-19
Silicon	Si	SiO_2	Silicon(IV)Oxide	+4	0.041	Cubic	4.17E-20
Chromium	Cr	Cr_2O_3	Chromium(III)Oxide	+3	0.063	BCC	1.39E-20
Iron	Fe	Fe_3O_4	Iron(II,III)Oxide	+2, +3	0.077	BCC	1.39E-20
		Fe_2O_3	Iron(III)Oxide	+3	0.064	BCC	1.39E-20

While the formation of copper (I) oxide is favored thermodynamically for the operating conditions, the unique oxidation state of copper in its oxide form at +1 may hinder it from participating in a co-precipitation reaction. Thus, it is argued that while the parabolic growth rate constant for copper (I) oxide is greater than that for the other alloying elements, it is unlikely that this oxide is produced.

Moreover, while the oxidation states of aluminum, vanadium, chromium, and iron are the same with

respect to plausible oxide formation, the rate of co-precipitation may be determined by the metal oxides with the slowest growth rate, which by the prediction of this model, are the oxides of chromium and iron. Thus, the low k_p values for oxides of iron and chromium obtained by this model may provide some explanation as to why the spinel layers analyzed in past experiments are primarily comprised of $(Fe_xCr_{1-x})_3O_4$ type oxides [31]. Furthermore, as shown in Table 14, the crystal structures of the chromium and iron oxides are alike which arguably promotes co-precipitation. The similar ionic radii of chromium and iron in the +3 oxidation state possibly facilitates combination of these elements into a single oxide. Thus, although aluminum and vanadium share oxidation states with iron and chromium, the difference in the ionic radii and corresponding oxide crystal structure can arguably preclude co-precipitation with iron and chromium. However, the oxidation states and crystal structures of vanadium and aluminum in their respective oxides coincide as well as those of silicon and tungsten. Niobium, manganese and nickel share oxidation states but do not share crystal structures in their corresponding oxides.

Two additional comments follow. Although scale removal is considered in the present model, it is only considered as a physical detraction from the total oxide layer thickness. Scale removal, however, also promotes oxidation by creating non-uniformities on the exposed surface of the metal oxide [4]. The scale removal experienced by the steels in the experiments conducted by Zhang [1] likely promoted and enhanced the oxidation rate. This provides another reason for the discrepancy between the experimentally determined and numerically determined k_p values. Also, as mentioned, the present model does not consider the outward diffusion of metal ions, which, depending on the operating conditions and type of oxide layer, can either contribute to or detract from the parabolic rate constant obtained in the present simulation.

To summarize, the numerically obtained k_p values for the individual oxides in the present model are assessed and reconciled with the experimentally determined k_p in terms of selective oxidation, co-precipitation, oxidation state and crystal structure, and scale removal.

Next, the relationship between the parabolic rate constant and oxygen diffusivity is discussed. Per the model proposed by Wagner [12], k_p is proportional to the average oxygen diffusion coefficient, $\bar{D}_{Ox}$ [32]. To be specific, solution of Fick's second law when the unexposed side of the plane is assumed to have zero oxygen concentration, in terms of δ and t, is given by:

$$\delta = 2\sqrt{\bar{D}_{Ox}t} \tag{75}$$

Solving equations (74) and (75) for k_p give the the relation

$$k_p = 2\bar{D}_{Ox} \tag{76}$$

46

By reversing the transformation on $\bar{D}_{Me}$ in equation (49), and assuming that $\bar{K}_r << \bar{V}_{OM}$, the diffusion coefficient of oxygen can be expressed by

$$\bar{D}_{Ox} = \frac{D_{Ox}}{m^2} \tag{77}$$

in which it recalled that m is dimensionless factor given by equation (18), the values of which are included in Table 11. The values for $\bar{D}_{Ox}$ are compiled in Table 15. A linear regression is applied to k_p versus $\bar{D}_{Ox}$ whereby equation eq. (78) is obtained.

$$k_p = 0.6121 \bar{D}_{Ox} \tag{78}$$

Table 15: Normalized Oxygen Diffusion Coefficient Values, $\bar{D}_{Ox}$

	Cu_2O	Al_2O_3	NbO	V_2O_3	MnO	NiO	WO_2	SiO_2	Cr_2O_3	Fe_2O_3	Fe_3O_4
$k_p (m^2/s)$	2.1956E-15	1.6533E-16	3.1667E-18	1.0833E-18	5.4167E-19	4.1667E-19	7.0833E-19	4.1667E-20	1.3889E-20	1.3889E-20	1.3889E-20
$D_{Ox}(m^2/s)$	3.5872E-15	2.6841E-16	5.2185E-18	1.6772E-18	9.0153E-19	1.0793E-18	6.8878E-19	4.7279E-20	1.4786E-21	3.1859E-23	2.9971E-23

A comparison of equations (78) and (76) indicates that, for a constant D_{Ox}, the values of k_p obtained from the present simulation are approximately three times less than those fitting an ideal parabolic growth. Once the convergence and stability criteria are determined for each oxide, plausible explanation for this is that the input value for D_{Ox}, estimated to be $1 \times 10^{-22}\,\mathrm{m^2/s}$ is an overestimation of the actual diffusivity oxygen within the oxide layer.

Finally, because D_{Ox} varies inversely with the square of w, so it follows for k_p. Thus, in this model, the k_p value will be higher for elements with lower weight ratios. This is the most direct explanation for the obtained k_p values.

5.2.3 Steady State Thickness

Discussion of the parabolic growth rate constant leads directly to the prediction of the steady state or asymptotic thickness, δ_s. Rearrangement of equation (71) gives

$$\delta_s = \frac{k_p}{K_r} \tag{79}$$

whereby δ_s is calculated with respect to the Tedmon oxidation-ablation model. For each oxide considered in the present simulation, δ_s is determined from the obtained values of k_p. These values are shown in Table 16. The experimental value for δ_s obtained by Zhang is $35.8\,\mu\mathrm{m}$ [1]. Without the consideration of stability and convergence criteria for the model, no direct conclusions can be made. It can be stated, however, that equation (79) shows that the values obtained for δ_s are proportional to the values obtained for k_p.

The approximation proposed by Zhang [1] in equation (73) is solved for δ_s by

$$\delta_s = \frac{2k_p t_{exp}}{3((2k_p t_{exp})^{\frac{1}{2}} - \delta_{exp})}.$$ (80)

For the experimental values, t_{exp} and δ_{exp}, the time and oxide layer thickness from the simulations run at the $250\,\mathrm{h}$ interval are substituted into equation (80). The results are also shown in Table 16. Both positive and negative values for δ_s are obtained. Referring back to Figure 18, it can be seen that the fitted parabolic curve at $250\,\mathrm{h}$ falls below the corresponding δ_{exp} values; in these cases, the denominator in (80) is rendered negative. As oxidation progresses, the experimental values should ideally fall below the increasing parabolic to reach an asymptotic thickness. Thus, in the incipient time region, without the optimization of stability and convergence, the approximation made by Zhang is not valid for the present model.

Table 16: Steady State Thickness, δ_s

micron	Cu_2O	Al_2O_3	NbO	V_2O_3	MnO	NiO	WO_2	SiO_2	Cr_2O_3	Fe_2O_3	Fe_3O_4
Zhang Appr.	6.845E+04	-2.898E+04	7.044E+02	-1.018E+02	5.956E+01	1.027E+01	6.147E+01	-3.731E+00	-4.110E+01	4.673E-01	4.673E-01
k_p/K_r		1.396E+04	1.052E+03	2.014E+01	6.890E+00	3.445E+00	2.650E+00	4.505E+00	2.650E-01	8.833E-02	8.833E-02	8.833E-02

5.2.4 Pilling-Bedworth Ratio

Discussion and consideration of a dimensionless quantity called the Pilling-Bedworth ratio follow. With respect to corrosion and oxidation, the Pilling-Bedworth ratio is the ratio metal oxide molar volume to that of the corresponding metal from which the oxide is created [33]. Historically, it had been one of the first methods of determining the likelihood of a stable oxide to form. The method to calculate the ratio, denoted R_{PB} is given by

$$R_{PB} = \frac{M_{oxide} \cdot \rho_{metal}}{\mathrm{n} \cdot M_{metal} \cdot \rho_{oxide}}$$ (81)

where M_{oxide}, M_{metal}, n, ρ_{oxide} and ρ_{metal} are the molar mass of the oxide, atomic mass of the respective metal, number of metal atoms per metal oxide molecule, oxide density and respective metal density. When this ratio falls within the region

$$1 < R_{PB} < 2$$ (82)

the oxide layer is considered to be passivating and prevents further oxidation [33]. When the ratio falls below this region, the oxide layer is considered too thin to offer any protection. Conversely, if the ratio is greater than this region, the oxide layer, while ample, is prone to chipping and erosion whereby protection is greatly reduced or removed [33].

The R_{PB} value was calculated for each of the oxides pertaining to this simulation. The ratios are listed in Table 17.

Table 17: Pilling-Bedworth Ratio

	Metal			Metal Oxide				
Element	Symbol	ρ_{metal} g/cm^3	M_{metal} g/mol	Molecular Formula	ρ_{oxide} g/cm^3	M_{oxide} g/mol	No. Metal Atoms/ Molecule Metal Oxide n	Pilling-Bedworth Ratio R_{PB}
Copper	Cu	8.96	63.546	Cu_2O	6	143.09	2	1.681310127
Aluminum	Al	2.7	26.981539	Al_2O_3	3.987	101.96	2	1.279530498
Niobium	Nb	8.57	92.90638	NbO	7.3	108.906	1	1.376145107
Vanadium	V	6.11	50.9415	V_2O_3	4.87	149.881	2	1.845682976
Manganese	Mn	7.21	54.93805	MnO	5.43	70.9374	1	1.71449989
Tungsten	W	19.25	183.85	WO_2	7.16	231.84	1	3.390333691
Nickel	Ni	8.908	58.6934	NiO	6.67	74.6928	1	1.699588745
Silicon	Si	2.329	28.085	SiO_2	2.196	60.08	1	2.268781376
Chromium	Cr	7.19	51.9961	Cr_2O_3	5.22	151.9904	2	2.013139079
Iron	Fe	7.874	55.847	Fe_3O_4	5.15	231.533	3	2.112905031
Iron	Fe	7.874	55.847	Fe_2O_3	5.24	159.69	2	2.148384449

Although more effective methods of predicting passivation capacity have been developed, the Pilling-Bedworth ratio gives a general idea of whether the surface area of the unoxidized metal will be completely covered by the resulting oxide. Within the region identified in equation (82), the entire surface area of the metal is predicted to be shielded by the oxide without the risk of the oxide layer being scaled off. Although all oxides in the layer are considered passivating, it has been stated that oxides for which the ratio is closer to 1 than to 2 are optimal due to compactness [4].

By this logic, the R_{PB} values of Al_2O_3 and NbO suggest that these oxides are optimal relative to oxides of other alloying elements. While it cannot be concluded that this is perhaps the reason for the value of experimental k_p and δ_s values reported by Zhang [1] falling between the numerical values of k_p and δ_s obtained in the present simulation for Al_2O_3 and NbO, future models could determine whether a correlation exists between the Pilling-Bedworth ratio and the values of the parabolic rate constant and the steady state thickness.

Chapter 6 Conclusions and Future Work

To summarize, the determination of the parabolic growth rate constant, k_p, for the oxides of each individual alloying metal of a metal alloy using the present numerical simulation can be a preliminary tool in characterizing the oxidation of the alloy in certain oxidizing environments. In the present study, the oxidation of stainless steel alloy EP-823 exposed to LBE in nuclear reactor coolant conditions is characterized. For each alloying metal of EP-823, its oxidation is numerically modeled using a finite difference method code, which tracks the concentration changes in a planar geometry with respect to space and time. By Fick's laws of diffusion, the oxidation of the element is linked to oxide layer thickness which in turn is fit to a parabolic growth law, the coefficient of which is the parabolic growth rate constant, k_p. The k_p values obtained for each alloying oxide are compiled and benchmarked with oxidation data from experiments conducted on EP-823 alloy. The experimental value of the k_p value falls within the range of k_p values obtained from the simulation for each alloying element. The benchmarked experimental value for steady state thickness is $35.8\,\mu m$, which is within the range of steady state thicknesses computed numerically per oxide of each alloying element.

Future work considering convergence criteria and optimization of stability for the simulation of the individual oxides are necessary to confirm and better assess the oxide layer growth model. Furthermore, an algorithm which allows for increased time intervals would allow for better compatibility between the numerical and benchmark values in determining the parabolic growth rate constant.

Moreover, a model considering temperature as an input could provide parabolic growth rate constant estimations at different temperatures whereby the activation energy, Q, of the oxidation reaction could be determined from the Arrhenius relation,

$$k_p = k_0 \exp \frac{-Q}{RT} \tag{83}$$

in which k_0 is the maximal growth constant. Models which consider other growth models such as linear, cubic, and logarithmic laws can also aid in the characterization oxidation reactions which do not fit the parabolic law.

As far as predicting effective oxidation, a model which simultaneously computes the contribution of each alloy to the complete oxide layer is ideal. This however, would require extensive study in electrochemistry, selective oxidation and co-precipitation, among other topics. The present model is deterministic; whether deterministic or stochastic models are ideal for simulating oxide layer growth can be researched.

Appendix A

Example of Non-Dimensionalizing a Governing Equation

(1) Advection-Diffusion Equation (Governing Equation):

$$\frac{\partial C_2(x,t)}{\partial t} = D_{Me}\frac{\partial^2 C_2(x,t)}{\partial x^2} - \left(\left(1 - \frac{1}{m}\right)V_{OM}(t + \Delta t) - \frac{K_r}{m}\right)\frac{\partial C_2(x,t)}{\partial x} \tag{A-1}$$

(2) x-domain:

$$\delta(t) < x < L(t) \tag{A-2}$$

(3) Boundary Conditions:

$$C_2(\delta(t),t) = C_{MO}, \quad C_2(L(t),t) = C_{M\infty} \tag{A-3}$$

(4) Initial Condition:

$$C_2(x,0) = 0, \quad 0 < x < \infty \tag{A-4}$$

(5) Define Dimensionless Variables.

$$\bar{t} = \frac{t}{t_n}, \bar{x} = \frac{x}{x_n}; \bar{C}_2 = \frac{C_2}{C_n}, \bar{t} = \frac{t}{t_n}, \bar{L}(\bar{t}) = \frac{L(t)}{L_n}, \bar{K}_r = \frac{K_r}{K_{rn}}, \bar{V}_{OM}(\bar{t}) = \frac{V_{OM}(t)}{V_{OMn}} \tag{A-5}$$

(6) Apply Chain Rule to (A-1). Simplify.

$$\frac{\partial C_2(x,t)}{\partial t} = \frac{C_n}{t_n}\frac{\partial \bar{C}_2(\bar{x},\bar{t})}{\partial \bar{t}}, \frac{\partial C_2(x,t)}{\partial x} = \frac{C_n}{x_n}\frac{\partial \bar{C}_2(\bar{x},\bar{t})}{\partial \bar{x}}, \frac{\partial^2 C_2(x,t)}{\partial x^2} = \frac{C_n}{x_n{}^2}\frac{\partial^2 \bar{C}_2(\bar{x},\bar{t})}{\partial \bar{x}^2} \tag{A-6}$$

(7) Substitute equation (A-6) into equation (A-1).

$$\frac{\cancel{C}_n}{t_n}\frac{\partial \bar{C}_2(\bar{x},\bar{t})}{\partial \bar{t}} = D_{Me}\frac{\cancel{C}_n}{x_n{}^2}\frac{\partial^2 \bar{C}_2(\bar{x},\bar{t})}{\partial \bar{x}^2} - \frac{\cancel{C}_n}{x_n}\left(\left(1 - \frac{1}{m}\right)V_{OMn}\bar{V}_{OM}(\bar{t}) - \frac{K_{rn}\bar{K}_r}{m}\right)\frac{\partial \bar{C}_2(\bar{x},\bar{t})}{\partial \bar{x}} \tag{A-7}$$

(8) Simplify.

$$\frac{x_n{}^2}{t_n D_{Me}}\frac{\partial \bar{C}_2(\bar{x},\bar{t})}{\partial \bar{t}} = \frac{\partial^2 \bar{C}_2(\bar{x},\bar{t})}{\partial \bar{x}^2} - \frac{x_n}{D_{Me}}\left(\left(1 - \frac{1}{m}\right)V_{OMn}\bar{V}_{OM}(\bar{t}) - \frac{K_{rn}\bar{K}_r}{m}\right)\frac{\partial \bar{C}_2(\bar{x},\bar{t})}{\partial \bar{x}} \tag{A-8}$$

(9) Choose Values for Characteristics.

$$x_n = L_0, t_n = \frac{L_0}{D_{Me}}, V_{OMn} = \frac{D_{Me}}{L_0}, K_{rn} = \frac{D_{Me}}{L_0} \tag{A-9}$$

(10) Substitute equation (A-9) into equation (A-8). Simplify.

$$\frac{\partial \bar{C}_2(\bar{x}, \bar{t})}{\partial \bar{t}} = \frac{\partial^2 \bar{C}_2(\bar{x}, \bar{t})}{\partial \bar{x}^2} - \left(\left(1 - \frac{1}{m}\right)\bar{V}_{OM}(\bar{t}) - \frac{\bar{K}_r}{m}\right)\frac{\partial \bar{C}_2(\bar{x}, \bar{t})}{\partial \bar{x}} \tag{A-10}$$

(11) Choose additional characteristic values.

$$\delta_n = L_0, C_n = C_{O0}, L_n = L_0 \tag{A-11}$$

(12) Substitute equation (A-11) into equations (A-2), (A-3), and (A-4).

$$\mathrm{x - domain:} \quad \bar{\delta}(\bar{t}) < \bar{x} < \bar{L}(\bar{t}) \tag{A-12}$$

$$\mathrm{BoundaryConditions:} \quad \bar{C}_2(\bar{\delta}(\bar{t}), \bar{t}) = \bar{C}_{MO}, \quad \bar{C}_2(\bar{L}(\bar{t})) = \bar{C}_{M\infty} \tag{A-13}$$

$$\mathrm{InitialCondition:} \quad \bar{C}_2(\bar{x}, 0) = 0, \quad 0 < \bar{x} < \infty \tag{A-14}$$

Appendix B

Derivation of Parabolic Growth Rate Due to the Diffusion of Oxygen

This derivation is based on Wagner's model of parabolic oxide layer growth [12]. Parabolic kinetics in oxidation occur when the oxide layer thickness grows in proportion to the square root of time. Here the diffusion of one of the reactants, the oxygen anions, is considered to determine the rate of the oxidation process. Thus, the oxide layer growth rate, given by the change in thickness, x, per change in time, t, is proportional to the flux of the oxygen anions, J_{0x}, through the oxide layer where:

$$\frac{dx}{dt} \propto J_{0x}. \tag{B-1}$$

Since J_{0x} can be defined by the product of concentration, C_{Ox}, and the velocity, V_{Ox}, of the oxygen ions, and V_{Ox} is proportional to the gradient of chemical potential, μ_{Ox}, of the ions, the flux of oxygen anions can be expressed by

$$J_{0x} = C_{Ox} B_{Ox} \frac{d\mu_{Ox}}{dx} \tag{B-2}$$

where B_{Ox} is the motility of the ions. The activity, or effective concentration, of the oxygen ions can be expressed in terms of chemical potential in two ways by [34]:

$$\mu_{Ox} = \mu_{Ox}{}^\circ + kT \ln a_{Ox} = \mu_{Ox}{}^\circ + kT \ln C_{Ox}. \tag{B-3}$$

Substitution of equation (B-3) into (B-2) gives

$$J_{Ox} = B_{Ox} kT \frac{d \ln C_{Ox}}{dx}. \tag{B-4}$$

By Wagner's model [32],

$$kT \frac{d \ln C_{Ox}}{dx} = kT \frac{dC_{Ox}}{dx} \tag{B-5}$$

Thus equation (B-4) becomes

$$J_{Ox} = B_{Ox} kT \frac{dC_{Ox}}{dx} \tag{B-6}$$

And substitution of equation (B-6) into equation (B-1) gives

$$B_{Ox} kT \frac{dC_{Ox}}{dx} = \frac{dx}{dt} \tag{B-7}$$

When the chemical potential, μ_{Ox}, is set as a constant at the boundaries of the oxide layer, then

$$\frac{dC_{Ox}}{dx} = \frac{\Delta C_{Ox}}{x}. \tag{B-8}$$

Substitution of equation (B-8) into equation (B-7) gives

$$B_{Ox}kT\frac{\Delta C_{Ox}}{x} = \frac{dx}{dt}. \tag{B-9}$$

By rearranging equation (B-9) and setting

$$B_{Ox}kT\Delta C_{Ox} = k_p, \tag{B-10}$$

where k_p is the parabolic rate constant, and applying a separation of variables followed by integration yields

$$x^2 = 2k_pt, \tag{B-11}$$

which is the parabolic rate law.

References

[1] J. Zhang, "Corrosion by liquid lead and lead-bismuth: Experimental result review and analysis," Los Alamos National Laboratory, LA-UR-08-07550 (2006).

[2] Mar 2017. [Online]. Available: http://www.g2mtlabs.com/corrosion/cost-of-corrosion/

[3] H. H. Uhlig and R. W. Revie, *Corrosion and corrosion control: An Introduction to Corrosion Science and Engineering.* Wiley, 1985.

[4] K. Mondal, Aug 2013. [Online]. Available: http://nptel.ac.in/courses/113104061/

[5] N. Sato, *Passivation of metals and semiconductors.* Pergamon Pr., 1990.

[6] T. Tan, "Modeling of the protective oxide layer growth in non-isothermal lead-alloys coolant systems," Ph.D. dissertation, University of Nevada, Las Vegas, 2007.

[7] J. Crank, *The Mathematics of Diffusion*, 1st ed. London: Clarendon Press, Oxford, 1956.

[8] A. Merimanov, *The Stefan Problem.* Walter de Gruyter Co., 1992.

[9] J. Hill, *One-Dimensional Stefan Problems: an Introduction.* Essex, England: Longman Scientific & Technical, 1987.

[10] H. Carslaw and J. Jaeger, *Conduction of Heat in Solids*, 2nd ed. Oxford University Press, 1946.

[11] L. Landau, "On the theory of phase transformations," *Zh. Eksp. Teor. Fiz.*, vol. 7, p. 19–32, 1937.

[12] C. Wagner, "The distribution of cations in metal oxide and metal sulphide solid solution formed during the oxidation of alloys," *Corrosion Science*, vol. 9, pp. 91–109, 1969.

[13] D. E. Coates and A. D. Dalvi, "An extension of the wagner theory of alloy oxidation and sulfidation," *Oxid. Met.*, vol. 2, p. 331, 1970.

[14] C. Tedmon Jr., H. Spacil, and S. Mitoff, "Cathode materials and performance in high-temperature zirconia electrolyte fuel cells," *J. Electrochem. Soc.*, vol. 116, pp. 1170–1175, 1969.

[15] Z. Ding and D. C. Lagoudas, "A domain transformation technique in oxygen diffusion problems with moving oxidation fronts on unbounded domains," *International Journal for Numerical Methods in Engineering*, vol. 42, no. 2, pp. 361–384, 1998.

[16] N. Shamsundar and E. Sparrow, "Effect of density change on multidimensional conduction phase change," *J. Heat Transfer*, vol. 98, pp. 550–557, 1976.

[17] S. Wong and C. Chan, "An improved formulation of the oxygen-diffusion problem and its application to zircaloy oxidation by steam," *Oxidation of Metals*, vol. 47, no. 5/6, 1997.

[18] P. Danckwerts, "Absorption by simultaneous diffusion and chemical reaction," *Transactions of the Faraday Society*, vol. 46, pp. 300–304, 1950.

[19] Y.-M. Sun, M.-T. Liang, and T.-P. Chang, "Time/depth dependent diffusion and chemical reaction model of chloride transportation in concrete," *Applied Mathematical Modelling*, vol. 36, no. 3, pp. 1114–1122, 2012.

[20] V. R. Voller, "Fast implicit finite difference method for the analysis of phase change problems," *Num. Heat Transfer*, vol. 17, pp. 155–169, 1990. [Online]. Available: https://ci.nii.ac.jp/naid/80005274756/en/

[21] J. Bunch and M. Mitchell, *Residual Effects on Fatigue and Fracture Testing and Incorporation of Results into Design.* ASTM International, 2007.

[22] H. Ellingham, "Reduciblity of oxides and sulfides in metallurgical processes," *Journal of the Society of the Chemical Industry*, vol. 63, pp. 125–133, 1944.

[23] *Handbook on Lead-bismuth Eutectic Alloy and Lead Properties, Materials Compatibility, Thermal-Hydraulics and Technologies.* OECD Nuclear Energy Agency, 2015.

[24] [Online]. Available: http://web.mit.edu/2.813/www/readings/Ellinghamdiagrams.pdf

[25] A. I. H. Committee, *ASM Handbook. Volume 3, Alloy Phase Diagrams*, 10th ed. ASM International, 1992, vol. 3.

[26] J. Gownia, *Metallurgy and Technology of Steel Castings.* Bentham Science Publisher., 2017.

[27] J. Robertson, "The mechanism of high temperature aqueous corrosion of stainless steels," *Corrosion Science*, vol. 32, p. 443, 1991.

[28] D. Peckner and I. Bernstein, *Handbook of Stainless Steels*, ser. McGraw-Hill Handbooks. McGraw-Hill, 1977.

[29] J. Castle and P. Surman, "The self diffusion of oxygen in magnetite," *Journal of Physical Chemistry*, vol. 71, pp. 4255–4259, 1967.

[30] G. S. G. Muller and F. Zimmermann, "Investigation on oxygen controlled liquid lead corrosion of surface treated steels," *Journal of Nuclear Materials*, vol. 85, p. 278, 2002.

[31] C. F. F. Barbier, G. Benamati and A. Rusanov, "Compatibility tests of steels in flowing liquid lead-bismuth," *Journal of Nuclear Materials*, p. 295, 2001.

[32] W. J. Moore, "Parabolic rate constants and diffusion mechanisms in oxides and sulfides," *Zeitschrift fur Elektrochunie*, pp. 794–795, 1958.

[33] N. Pilling and R. E. Bedworth, "The oxidation of metals at high temperatures," *J. Inst. Met.*, vol. 29, pp. 529–591, 1923.

[34] "Thermodynamic activity," Apr 2018. [Online]. Available: https://en.wikipedia.org/wiki/Thermodynamic activity

Curriculum Vitae

Name	Rajyalakshmi Palaparty
Contact Information	rajya.palaparty@gmail.com

Overview of Education	Bachelor of Science Mechanical Engineering University of Nevada, Las Vegas 2015 Master of Science Mechanical Engineering University of Nevada, Las Vegas 2018 (Expected)

Academic & Related Employment	Mathematics Tutor Academic Success Center University of Nevada, Las Vegas September 2016 - Present Mathematics & Science Tutor Grade Potential Tutoring Las Vegas, NV June 2013 - Present SAT/ACT/MCAT/GRE Tutor Excel Academy Las Vegas, NV June 2015 - June 2016 Mathematics and Physics Tutor Mathease Tutoring Henderson, NV June 2013 - Present	Tutor Department of Mechanical Engineering University of Nevada, Las Vegas June 2017 - Present Teaching Assistant, Automatic Controls Laboratory Department of Mechanical Engineering University of Nevada, Las Vegas Fall Semester 2016/2017 Grader, Engineering Thermodynamics I Department of Mechanical Engineering University of Nevada, Las Vegas Fall Semester 2017

Research Projects	Nuclear Energy University Program University of Nevada, Las Vegas Sequestration of Technetium in Ceramic Forms September 2015 - August 2016

Conference Paper	Thomas Hartmann, Rajyalakshmi Palaparty, Florian Wolke. "Fabrication and Properties of Advanced Ceramic Technetium Waste Forms," Proceedings of 2017 WM Symposia, March 5-9, 2017, Phoenix, Arizona, USA.

Master's Thesis Title	NUMERICAL STUDY OF OXIDATION IN STAINLESS STEEL ALLOY EP-823 BY LIQUID LEAD-BISMUTH EUTECTIC